Experimental simulation of magma-carbonate interaction beneath Mt. Vesuvius, Italy

Jolis E. M.[a]*, Freda, C.[b], Troll V. R.[a,b], Deegan F. M.[a,c], Blythe, L. S.[a], McLeod, C.L.[d,e], Davidson, J. P.[d]

[a]Dept. of Earth Sciences, CEMPEG, Uppsala University, Villavägen 16, SE-752 36 Uppsala, Sweden
[b]Istituto Nazionale di Geofisica e Vulcanologia, Via di Vigna Murata 605, 00143 Roma, Italy
[c]Dept. of Geosciences, Swedish Museum of Natural History, SE-104 05 Stockholm, Sweden
[d]Dept. of Earth Sciences, Durham University, Science Labs, Durham DH1 3LE, UK
[e]Dept. of Earth and Atmospheric Sciences, University of Houston, Houston, Texas 77004

*Corresponding author: EMJ (ester.jolis@geo.uu.se)

Abstract

We simulated the process of magma-carbonate interaction beneath Mt. Vesuvius in short duration piston cylinder experiments under controlled magmatic conditions (from 0 to 300 s at 0.5 GPa and 1200 °C), using a Vesuvius shoshonite composition and upper crustal limestone and dolostone as starting materials. Backscattered electron images and chemical analysis (major and trace elements and Sr isotopes) of sequential experimental products allow us to identify the textural and chemical evolution of carbonated products during the assimilation process. We demonstrate that melt-carbonate interaction can be extremely fast (minutes) and results in dynamic contamination of the host melt with respect to Ca, Mg and $^{87}Sr/^{86}Sr$, coupled with intense CO_2 vesiculation at the melt-carbonate interface. Binary mixing between carbonate and uncontaminated melt cannot explain the geochemical variations of the experimental charges in full and convection and diffusion likely also operated in the charges. Physical mixing and mingling driven by exsolving volatiles, seems to be a key process to promote melt homogenisation. Our results reinforce hypotheses that magma-carbonate interaction is a relevant and ongoing process at Mt. Vesuvius and one that may operate not only on a geological, but on a human timescale.

Keywords: Mt. Vesuvius, magma-carbonate interaction, crustal assimilation, CO_2 liberation, experimental petrology

1. Introduction

The Mt. Somma-Vesuvius complex (1281 m a. s. l.) comprises Mt. Somma, the > 25 to 14 kyr strato-volcano, and Mt. Vesuvius, the recent cone which has grown within the older Mt. Somma caldera (e.g., Rolandi et al. 2004; Peccerillo, 2005; Piochi et al. 2006; Di Renzo et al. 2007) and which we collectively term the "Vesuvius volcanic system" (VVS). The VVS is characterised by variable types of eruption, ranging from effusive lava emission to explosive strombolian, sub-plinian and plinian events (Orsi et al. 1996; Peccerillo 2005; Paone 2006; Piochi et al. 2006). The VVS is sited on a sequence of Mesozoic and Cenozoic carbonates overlain by the Miocene siltstone sediments of the Campanian Plain (Brocchini et al. 2001; Civetta et al. 2004; Del Pezzo et al. 2006). Seismic tomography studies have suggested that the top of the Mesozoic carbonate basement lies at around 2.5 - 3 km depth underneath the volcano (Zollo et al. 2002). The level at ~ 8 - 11 km depth has also been identified as a discontinuity, likely representing the top of the present day magma reservoir, which is probably linked to the base of the Mesozoic carbonate sequence at ~ 10 - 11 km depth (Zollo et al. 1996; Berrino et al. 1998; Auger et al. 2001). The VVS has been the focus of attention ever since the famous AD 79 eruption, being one of the most hazardous volcanic systems in Europe due to the densely populated Neapolitan region in its shadow. Although much is known concerning the volcano and its internal workings, a comprehensive understanding of the role of magma-crust interaction processes at the VVS has not yet been achieved.

The VVS produces slightly silica-undersaturated K-basalts and K-trachytes to highly silica-undersaturated K-tephrites and K-phonolites (D'Antonio et al. 1999; Paone 2006; Piochi et al. 2006). The compositional variability of these magmas has been attributed to: ***i*)** mantle source variability (e.g., Ayuso et al. 1998; Peccerillo 1999; Somma et al. 2001), ***ii*)** differentiation and magma mixing (e.g., Turi and Taylor 1976; Civetta el at. 1991) and ***iii*)** contamination through carbonate assimilation (e.g., Rittmann, 1933; Fulignati et al. 1995; Del Moro et al. 2001; Gilg et al. 2001). The role of carbonate assimilation has recently been documented for a

significant number of volcanic systems emplaced in carbonate-rich crust, e.g., Popocatepetl, Colli Albani, and Merapi (e.g., Goff et al. 2001; Dallai et al. 2004; Schaaf et al. 2005; Chadwick et al. 2007; Freda et al. 2008). In fact, carbonate assimilation has been shown to occur over short timescales (minutes in experiments) and thus the effect of carbonate decomposition in natural systems is thought to release significant amounts of CO_2 on timescales of hours to days (Deegan et al., 2010, 2011; Troll et al., 2012a). Such CO_2 influx into a volcanic system may not only have the potential to modify magma composition but also the style of eruptive activity (Deegan et al. 2010, 2011; Dallai et al. 2011; Freda et al. 2011; Troll et al. 2012a, b). At the VVS, the presence of a thick carbonate basement, the frequent occurrence of skarn xenoliths, and the anomalous gas chemical compositions unequivocally suggest that contamination through carbonate assimilation is a relevant process and may play an important role in the volcano's magma evolution and its eruptive behaviour and styles (cf. Freda et al. 1997; Del Moro et al. 2001; Gilg et al. 2001; Fulignati et al. 2004, 2005; Iacono-Marziano et al. 2009; Dallai et al. 2011). In this study, we report on a set of experiments designed to examine magma-carbonate interaction processes under controlled conditions (0.5 GPa and 1200 °C), employing a composition representative of primitive VVS magmas and various local carbonates. Previously, magma-carbonate interaction experiments were run over hours to days to establish mineral phase relationships and the liquid line of descent in magmatic products affected by carbonates (e.g., Freda et al., 2008; Iacono Marziano et al. 2008; Mollo et al. 2010). In contrast, our experimental series is designed to perform very short duration experiments (0, 60, 90 and 300 s; cf. Deegan et al. 2010), allowing the preservation of textures and phases developed during progressive carbonate break-down and degassing. Coupled with *in-situ* elemental and Sr-isotope constraints on our experiments, our data provide a more comprehensive understanding of the dynamics of magma-carbonate interaction in the VVS.

2. Experimental methods

The experiments were conducted in an end-loaded piston-cylinder apparatus at the HP-HT Laboratory of Experimental Volcanology and Geophysics of Istituto Nazionale di Geofisica e Vulcanologia (INGV, Rome, Italy). Experiments were carried out at 0.5 GPa equivalent to ca. ~ 13 - 14 km depth. This is the lowest pressure to which this end-loaded piston-cylinder apparatus is calibrated for, but is similar to the pressure inferred for the VVS magma reservoir (≥ 10 km depth; Zollo et al. 1996, 1998; Auger et al., 2001). The experimental temperature of 1200 °C was calculated as the liquidus temperature of the starting composition at 0.5 GPa and initial water content of 2 wt. %, using the MELTS algorithm (Ghiorso et al. 1994). The experimental temperature was reached in 6 minutes, which is sufficiently fast to preserve the textural relationship of the carbonate phase in the shortest duration experiments and allow inspection of the interaction between carbonate and the resulting melts in detail (see Deegan et al. 2010). Our experimental approach thus approximates the likely physical and chemical conditions of direct magma-carbonate interaction in the VVS.

The starting materials used in our experiments were a shoshonitic lava flow from the VVS (Di Renzo et al. 2007) and limestone and dolostone from the local Procida carbonate formation (e.g., Barberi et al. 1981; Civetta et al. 1991). The shoshonitic lava flow represents one of the least evolved rocks outcropping in the Neapolitan area. A shoshonite sample was first crushed, powdered, and doped with 2 wt. % H_2O (added by microsyringe into an experimental capsule) and then melted at 1250 °C and 0.5 GPa to produce a hydrated shoshonite glass. The hydrated glass was analysed for its major element composition (see **Table 1**) and was verified to be free of crystals and crystallites. Then, the hydrated shoshonite glass was powdered and used as the magmatic starting material in our experimental series.

The hydrated shoshonite powder was placed in platinum capsules (3.0 mm diameter, 12.0 mm long) together with fragments of ~ 6 - 8 mg (≤ 3.0 mm side length) of either limestone or dolostone (**Table 1**). The capsules were then welded shut and positioned in tandem into a 19.1 mm NaCl-crushable alumina-pyrex assembly. This means that the two capsules were placed

side by side in the same assembly, one containing the hydrated shoshonite glass and limestone and the other the hydrated shoshonite glass and dolostone. The tandem approach has the advantage that it allows a direct comparison between limestone- and dolostone-bearing experiments as physical parameters (pressure, temperature and time) are otherwise identical. The capsules were surrounded by pyrophyllite powder to prevent water loss (see Freda et al., 2001) and further details of the experimental approach can be found in Freda et al. (2008) and Deegan et al. (2010).

3. Analytical Methods

The experimental products were analysed using a JEOL-JXA8200 electron microprobe (EMPA) and a JEOL-6500F field emission scanning electron microscope (FE-SEM) at INGV Rome. Microprobe analyses were performed using an accelerating voltage of 15 kV, a beam current of 5 nA, and a beam diameter of 5 μm for glass and 1 μm for mineral analyses (see, e.g., Iezzi et al., 2008, for analytical details). Sodium and potassium were analysed first to reduce possible volatilisation effects. The average standard deviation (1σ) of major element oxides (in wt. %) is 0.34 for SiO_2, 0.06 for TiO_2, 0.11 for Al_2O_3, 0.10 for FeO, 0.03 for MnO, 0.07 for MgO, 0.16 for CaO, 0.05 for Na_2O, 0.03 for K_2O, 0.04 for P_2O_5.

Micro-sampling of the experimental products for their Sr isotope ratios was performed at the Arthur Holmes Isotope Laboratory, Department of Earth Sciences, Durham University, UK using a New Wave Micromill™ and following the technique outlined in Charlier et al. (2006). The Micromill consists of a binocular microscope, a mill, a stage, which controls movement reproducible to ± 1 μm, and a computer workstation which integrates all the components (Charlier et al. 2006). Sampling sites were selected using BSE images to precisely locate the drill points and avoid fractures and bubbles. The samples were milled along selected areas to a depth of 30 μm. Milling was carried out under a single drop of Milli-Q water to collect the drilled sample dust. The sample and Milli-Q water mixture was pipetted off and transferred directly to a ‘gold boat’ for processing and micro-Sr column chemistry as described in

Charlier et al. (2006). After processing, the samples were analysed by TIMS using a Thermo-Finnigan Triton system (see Font et al. 2008). During the analysis period (July to August 2010) the international Sr standard NBS-987 was analysed with sample sizes ranging from 3 ng to 600 ng. The overall average Sr isotopic ratios for the NBS-987 measurements during this period (n = 26) was 0.710261 ± 0.000016, within error of the published $^{87}Sr/^{86}Sr$ value of 0.710248 ± 0.000023 (2σ) (n = 427) reported by Thirlwall et al. (1991). Aliquots of the dissolved milled samples were analysed for their trace element concentrations by inductively coupled plasma mass spectrometry (ICP-MS) using a Thermo Electron Element II system at Durham University, UK. Procedural details are provided in Font et al. (2008). Total procedural blanks (n = 5) were less than 22 pg for all elements analysed. Sr blanks averaged 0±1pg (2σ, n = 5).

4. Results

4.1. *Features of the experimental products*

The experimental conditions for all ten experiments are given in **Table 2** and representative electron microprobe analytical traverses of two experimental products are reported in **Table 3**. Three major phases were identified: ***i)*** two distinct glasses (representing melts), Ca-normal and either Ca- or Ca-Mg-rich, which are identified in BSE images as dark and bright in colour, respectively. A contamination front (CF) usually separates the two glass domains (**Fig. 1)**. ***ii)*** Crystalline phases, such as calcite, pyroxene and olivine (**Figs. 2 and 3),** and ***iii*)** a vapour phase represented by bubbles (e.g., **Fig. 1)**. In the following section the main features of the experimental products are described to explain the dynamics of magma-crust interaction in the experiments and to report on the differences between limestone- and dolostone-bearing experiments.

Limestone-bearing experiments

In the limestone-bearing experimental products, for t_d = 0 to 90 s, two distinct glass regions were observed (**Fig. 1a-c**): ***i)*** a Ca-normal glass domain, very similar in composition to the shoshonite starting material (av. 49.85 wt. % SiO_2, 9.98 wt. % CaO) and ***ii)*** a Ca-rich glass domain with an interface between the two (CF). Within the CF region, the Ca-normal glass domain shows progressive depletion in silica and enrichment in CaO, grading into the Ca-rich melt domain (**Fig. 4**), with aluminium strongly mimicking the behaviour of silica. The interfacial regions (CF) hence involve progressive physico-chemical mixing between the two dominant glass domains and an interfacial boundary between the Ca-rich and Ca-normal domains is observed in all experiments. The solid phases are dendritic micro-crystals of calcite (**Fig. 2**) produced in Ca-rich areas of the Ca-rich glass domains. These crystals represent quench crystals formed from local enrichment of former calcite components in the experimental melts. Notably, the t_d = 300 s run is characterised by a more homogeneous Ca-rich glass, vapour (bubbles) and no crystals (**Fig. 1d**).

Dolostone-bearing experiments

The dolostone-bearing experimental products contain either glass and vapour phases (t_d = 0 s; **Fig. 1e)** or crystals, glass and vapour phases (t_d = 60 to 300 s; **Fig. 1f-h)**. The results of chemical traverses through the various glass regions are shown in **Figure 5**. The dolostone-bearing experiments show a normal glass with chemical composition similar to the starting material, a contaminated glass (Ca-Mg enriched), and CF regions in between the two. In the CF areas, it is possible to distinguish a progressive dilution of silica and coeval calcium and magnesium enrichment relative to the shoshonite starting material (**Fig. 5**). Crystalline phases in the dolostone-bearing experiments are ferromagnesian olivine and pyroxene. Analyses of all mineral phases are provided in the Online Resource 1 (**Table OR1**). The ternary diagram in **Figure 3** shows the crystalline phases in the Ca_2SiO_4 - Mg_2SiO_4 - Fe_2SiO_4 and in the $CaSiO_3$ - $MgSiO_3$ - $FeSiO_3$ systems. Pyroxene is dominant over olivine and is highly enriched in CaO (> 20 wt %) and MgO (10.01 - 13.16 wt. %), in agreement with its occurrence in the

interfacial area, i.e., depletion in SiO_2 and enrichment in CaO, MgO and Al_2O_3 (**Fig. 3a)**. The olivine compositions are close to forsterite ($Fo_{95-97.5}$), but with a notable enrichment in CaO (1.31 to 2.36 wt %; **Fig. 3b)** and thin Fe-rich, likely more outer rims. The olivine crystals (~ 10 - 20 μm size) are euhedral and the pyroxene display euhedral to subhedral shapes, which points to direct growth of olivine and pyroxene from contaminated melts (**Fig. 3**).

Vapour phase in experimental products

The vapour phase in our experiments is preserved as numerous vesicles (bubbles) that formed at the contamination front predominantly from exsolved CO_2 (see below). Vesicles were observed in all experimental runs in different quantities, sizes and spatial distributions. For dolostone-bearing experiments, the vesicles' spatial distribution is not random, rather the bubbles tend to concentrate close to contaminated areas. In contrast, for limestone-bearing experiments the bubbles have a tendency to nucleate in the Ca-rich melt domains and migrate into the Ca-normal glass as reflected by different generations of vesicles and micro-bubble fronts (**Fig. 1**). Bubble sizes increase from a micrometer to a millimetre scale with progressive experimental run-time (Blythe et al. 2012), reflecting initial bubble nucleation that is followed by progressive bubble growth and coalescence.

4.2. Strontium isotope compositions in the experimental products

The Sr isotope variations in limestone- and dolostone-bearing experiments are illustrated in **Figures 6** and **7** and the data are reported in **Table 4**. All trace element concentrations in the drilled samples can be found in the Online Resource 2 (**Table OR2**). The micro-Sr-isotope analyses show significant $^{87}Sr/^{86}Sr$ variability in each experiment (0.706729±10 to 0.707023±33 in limestone-bearing and 0.707017±8 to 0.707743±10 in dolostone-bearing experiments). The analysed Ca-normal glass has low $^{87}Sr/^{86}Sr$ values (0.706729±10 to 0.706896±40) similar to those of the shoshonite starting material (0.706661±8; Di Renzo et al. 2007). In contrast, the more radiogenic $^{87}Sr/^{86}Sr$ values (0.706951±17 to 0.707743±10) correspond to Ca- or Ca-Mg-rich domains, with $^{87}Sr/^{86}Sr$ ratios that trend towards those of the

carbonates of the Campanian region (0.7072±1 to 0.7093±8; Civetta et al. 1991; Piochi et al. 2006; Iannace et al. 2011). Three of the microdrilled experiments were analysed in the CF, showing $^{87}Sr/^{86}Sr$ signatures that fall in between the respective Ca- or Ca-Mg-rich and Ca-normal glass compositions of these experiments (**Figs. 6 and 7**).

5. Discussion

5.1. Effects of magma-carbonate interaction

Magma-carbonate interaction and consequent carbonate assimilation allows for several possible reaction routes, ranging from direct dissolution to formation of a series of intermediate products, such as the various skarn assemblages frequently observed (e.g., Gaeta et al. 2009; Mollo et al. 2010; Troll et al. 2012b). The net result of this interaction is an overall release of CaO by limestone and CaO and MgO by dolostone into the host magmas(s), and associated liberation of CO_2 (cf. Mollo et al. 2012; Troll et al. 2012a). The experiments simulate direct magma-carbonate interaction, which is demonstrated by the chemical profiles and by the abundant occurrence of bubbles in the experimental products. A recent experimental investigation using a basaltic-andesite composition from Merapi volcano and Indonesian carbonate as starting material, and employing analogous pressure (0.5 GPa), temperature (1200 °C) and water content (~ 2 wt. %), showed similar processes of magma-carbonate interaction at work (Deegan et al. 2010). These authors established that carbonate break-down began during the experimental heating phase (approximately 6 min.) and the time required for complete carbonate assimilation was probably no more than ca. 330 s at their target experimental conditions. In contrast to the Merapi experiments, we observe that no original carbonate is preserved in any of our experimental products (**Figs. 1 and 2**), implying that carbonate dissociation and complete dissolution occurred before the target temperature of 1200 °C was reached. The highest degree of physico-chemical mixing between melt domains occurs between t_d = 60 and 90 s (i.e., mixing initially increases with time; **Figs. 8 and 9**). At t_d ~ 300 s, contaminated melt dominates almost the entire volume of the experimental charge,

leaving normal melts at the rims only, i.e., mixing is approaching completion. It should be noted though that calcite (or alternatively pyroxene and olivine) crystallised where local enrichment of certain elements was the result of magma-carbonate interaction and implies that chemical homogenisation between melts is limited within the timeframe of our experiments, i.e., the run-time for the experiments does not permit complete homogenisation. The Vesuvius experiments, in contrast to the Merapi ones, therefore display a significantly shorter timescale of magma-carbonate interaction, suggesting faster reaction rates between the shoshonite melt and the carbonate (limestone and dolostone) under otherwise similar pressure and temperature conditions.

The chemical variations between glass domains in limestone- and dolostone-bearing experiments can be approximated by binary mixing models with the starting materials (limestone, dolostone and shoshonite) as end-members. Based on these models, we provide an estimate of the maximum degree of mixing between melts in each experimental step. The degree of mixing varies mainly with the experimental duration (t_d) (**Figs. 8 and 9**) and maximum mixing degrees are often confined to spatially limited zones of about 100-200 μm in experiments up to 90 s (**Figs. 4 and 5**).

The limestone-bearing experiments reflect this variation on the maximum degree of mixing between carbonate and shoshonite through time (**Fig. 8;** see **Online Resource 3 Fig OR1**) and similar degrees of mixing are observed for elements such as MgO, Al_2O_3 or NaO_2. The maximum degree of limestone component in the melt phase (limestone: shoshonite, weight ratio) is ***i)*** ~ 40:60 at t_d = 0 s, ***ii)*** ~ 50:50 at t_d = 60 s, and ***iii)*** ~ 60:40 at t_d = 90 s. At ***iv)*** t_d = 300 s, the resultant melt is almost homogenous, representing a mixture between dissolved carbonate and shoshonite melt of about 25:75. For the dolostone-bearing experiments, the maximum degree of dolostone component in the melt phase (dolostone: shoshonite, weight ratio) for experimental duration is (**Fig. 9;** see **Online Resource 3 Fig OR2): *i)*** ~ 15:85 at t_d = 0 s, ***ii)*** ~ 45:55 at t_d = 60 s, ***iii)*** ~ 45:55 at t_d = 90 s, and ***iv***) about 25:75 at the longest

experimental duration of 300 s. These models demonstrate that the degree of mixing is time-dependent and generally greater for the longer duration experiments. For the experiments between 0 and 90 s, the resultant melts are inhomogeneous and in disequilibrium since the system undergoes various degrees of diffusive and convective mixing in addition to crystal growth and resorption (e.g., calcite, pyroxene and olivine). In contrast, at t_d = 300 s, in both limestone- and dolostone-bearing experiments, a hybrid melt containing about 25 wt. % CaO begins to form as the result of pervasive mixing and progressive homogenisation (**Figs. 8 and 9; Online Resource 1**). Pure binary mixing between two melt end-members should follow a linear relationship for a regular element pair (e.g., CaO vs. SiO_2), which, however, is not always observed in our experiments (**Figs. 8 and 9**). The observed variations may reflect different mobility of trace and major elements over very short timescales during incipient mingling and mixing, producing complex and fluctuating patterns that deviate from straight mixing trends. This deviation is most pronounced in the dolostone-bearing experiments, however, where the mixing trajectory appears to move furthest from the straight mixing trend, probably a result of crystal growth (olivine and pyroxene) and associated Mg removal from the melt that will shift the Ca/Mg ratio of the melt away from that of an ideal mixture (De Campos et al. 2008; Perugini et al. 2006, 2008). We also estimated "apparent diffusivities" of SiO_2, Al_2O_3, MgO and CaO across the contamination front in the limestone-bearing experiments (see **Online Resource 4)**. The results yield apparent diffusivities in m^2/s of $8.5 \cdot 10^{-10}$ to $8.6 \cdot 10^{-7}$ for SiO_2, $8.5 \cdot 10^{-10}$ to $1.9 \cdot 10^{-9}$ for Al_2O_3, $8.5 \cdot 10^{-10}$ to $1.1 \cdot 10^{-8}$ for MgO and $3.4 \cdot 10^{-11}$ to $6.3 \cdot 10^{-6}$ for CaO in the 60 and 300 s experiments, respectively (**Online Resource 4**). The determined values are between two and five orders of magnitude greater than well-established diffusivities for these elements (e.g., Watson 1982; Watson and Jurewicz 1984; Baker 1991; Lesher et al. 1996; Liang et al 1996; Zhang 1993 and 2010) and, moreover, they vary between the different duration experiments. These data imply that although diffusion is a relevant process at play, the overall elemental gradients observed must

be the result of a combination of processes including mingling, mixing, convection, and local crystal growth (**Figs. 1, 8 and 9**). These additional processes can all affect the melt interface and thus overprint diffusion profiles in the experimental charges. In our experiments, the process of physical mixing and mingling observed between the melt domains is driven by volatiles that exsolve during carbonate assimilation (**Fig. 1**), which likely contributes most strongly to melt homogenisation on the timescale of our experiments. Crystal growth, on the other hand, is influenced by carbonate break-down in our experiments. Limestone, for example, contributes to local calcite-saturation whereas dolostone provides additional CaO and MgO thereby promoting crystallisation of Ca-rich pyroxene and Ca-Mg-rich olivine (cf. Metz and Milke, 2012). The crystallisation of these mineral phases in our experiments is a function of the state of the contaminated melt, i.e., it is dependent on melt domains that are locally enriched in CaO and MgO prior to full homogenisation. Notably, the growth of high-Mg olivine from dolostone contaminated melt raises the possibility that high-Fo olivine is not always an indicator for primitive or primary magma compositions in volcanic systems and particularly not in the VVS.

5.2. $^{87}Sr/^{86}Sr$ composition of the experimental products

The $^{87}Sr/^{86}Sr$ isotope variations provide a first order approximation of the degree of carbonate assimilation in our experiments. The Sr isotope ratios and Sr concentration for Mt. Vesuvius shoshonitic magmas range between 0.7067 and 0.7071 and from 735 to 1093 ppm, respectively (Di Renzo et al. 2007). The $^{87}Sr/^{86}Sr$ isotope ratios and Sr concentration of carbonate-rich lithologies from the Campanian region were previously thought to range between 0.7075 and 0.7090 and from 500 to 1000 ppm, respectively (Civetta et al. 1991; Piochi et al. 2006; Del Moro et al. 2001). More recent studies on the same carbonates now also report lower values of $^{87}Sr/^{86}Sr$ to be present, e.g., 0.7072 to 0.7074 (Iannace et al. 2011) with associated Sr concentrations of as little as 41 to 151 ppm, implying that these carbonates are highly heterogeneous in their Sr concentrations and $^{87}Sr/^{86}Sr$ composition (see below).

The Sr-isotope profiles of the experimental products display a broad correlation of higher $^{87}Sr/^{86}Sr$ ratios with increasing CaO wt. %, i.e., with the most contaminated drill samples, whereas the non-contaminated glasses show Sr isotope ratios that overlap with those of the natural shoshonite starting material (**Fig. 10a**). The $^{87}Sr/^{86}Sr$ ratios observed in the CF regions usually fall in between these extremes and frequently form mixtures with intermediate $^{87}Sr/^{86}Sr$ signatures (**Figs. 6 and 7**). Indeed, in this respect, the isotopic variations observed within each individual experiment can be explained as the result of mixing between "normal" and "contaminated" melts. The situation appears somewhat more complex, however, when using binary mixing trajectories between the published values for the shoshonite and for the various carbonate $^{87}Sr/^{86}Sr$ values as well as for a high (500-1000 ppm) and a low (<500 ppm) Sr concentration group that are now available in the literature (e.g., Civetta et al. 1991; Piochi et al. 2006; Del Moro et al. 2001; Di Renzo et al., 2007; Iannace et al. 2011). For the VVS shoshonite, a $^{87}Sr/^{86}Sr$ ratio of 0.7067 and Sr concentration of 735 ppm was chosen (**Table 1**). For the carbonates, five values were selected (C_1-C_5) because their Sr-isotope ratios are so variable that our single compositions cannot represent the available data range on limestone and dolostone from the Campanian region. For example, the high Sr concentration carbonate (500-1000 ppm) cannot explain the range of Sr isotopic values measured in the experiments as only one drill sample, the most radiogenic one (D-V2.4, 0.707743), falls into the shoshonite – C_1– C_2 – mixing space (**Fig. 10b**). The best fit for the remaining drill data is achieved using low Sr (<500 ppm) carbonates (C_2-C_5). Employing these possible end-member(s), all remaining experimental data fall into the theoretically possible mixing space. This observed range of $^{87}Sr/^{86}Sr$ in the experimental Ca-rich melts implies that on the one hand the contaminant used in our experiments is highly inhomogeneous on a mm to sub-mm-scale, which is consistent with the realisation that the Campanian carbonates are heterogeneous regarding their Sr-isotope values as well as their Sr-concentrations (e.g., Iacono-Marziano et al. 2008; Iannace et al. 2011). On the other hand, most carbonate material in our experiments

appears to have lower Sr concentrations than the shoshonite melt (see **Table 1;** Di Renzo et al., 2007). A contaminated shoshonite may therefore be less radiogenic than previous predictions of contamination had suggested on the basis of the high $^{87}Sr/^{86}Sr$ and Sr concentration values available for the Procida formation at that time (e.g., Ayuso et al. 1998; Iacono-Marziano et al. 2008). Considering the full range of possible mathematical solutions, including the new low Sr and low $^{87}Sr/^{86}Sr$ end-members (Iannace et al. 2011; **Table 1**), the most intensely contaminated experimental drill-samples then calculate to mixtures of up to between 55 and 75% carbonate-derived $^{87}Sr/^{86}Sr$ relative to unmodified shoshonite (**Fig. 10b**). The noteworthy aspect of these results is that relatively primitive compositions at the VVS (e.g., shoshonite) may represent contaminated magma even in the absence of particularly high Sr-isotope ratios or high Sr elemental concentrations, as large amounts of contamination by a low $^{87}Sr/^{86}Sr$ and low Sr ppm carbonate will only exhibit a small effect on the Sr isotope composition of the magma. A CaO and Sr relationship, as previously predicted for substantial limestone assimilation, cannot be expected if low-Sr isotope contaminants and variable Ca and Mg ratios in limestones versus dolostones (and their resulting calc-silicate skarns) are considered to influence the system in addition to pure limestone uptake. The lack of a clear CaO-Sr relationship is hence not an argument against carbonate assimilation (cf. Ayuso et al. 1998). Coupled with the occurrence of high-Mg olivine and pyroxene in our dolostone-bearing experimental products, a mineral association known to occur in some primitive VVS samples (e.g., Dallai et al. 2011), low-Sr dolostone may in fact be a key contaminant for the VVS.

5.3. CO_2 liberation during magma-carbonate interaction

Dissolved volatiles in silicate melts play an important role in defining physical properties of magmas for, e.g., density, viscosity, vesicularity, and thus influence ascent behaviour and eruptive styles (e.g., Dingwell 1996; Baker et al. 2005; Deegan et al. 2010; Lesne et al. 2010). The most abundant volatiles in magmas are H_2O and CO_2, which are commonly dissolved in

different percentages depending on melt composition, pressure, temperature and degree of saturation (e.g., Zhang and Stolper 1991). In particular, solubility experiments on shoshonite under conditions similar to those used in this study, i.e., 1250 °C and 0.4 GPa, show that water solubility is about 8 wt. %, while CO_2 solubility is limited to < 3000 ppm. Under CO_2 saturated conditions (> 3000 ppm), only 2 wt. % H_2O is soluble, however (Di Matteo et al. 2006; Vetere et al. 2011). This is broadly consistent with H_2O and CO_2 solubilities predicted for shoshonite by the numerical model of Papale et al. (2006), which yields solubilities of 1.9 wt. % and 3449 ppm for H_2O and CO_2, respectively, at the pressure and temperature conditions of our experiments. In our experiments, therefore, H_2O and CO_2 coexist in the melt. During carbonate break-down and assimilation, the progressive increase of CaO and CO_2 in the melt will affect both the CO_2 and H_2O solubilities (see **Table 3;** Holloway 1976; Watson et al. 1982; Blank and Brooker 1994; Holloway and Blank 1994; Dixon 1997; Botcharnikov et al. 2005; Moore, 2008) and will provide CO_2 to the melt until volatile saturation is achieved. At this point, a fluid phase will form that will likely contain only a small portion of H_2O since the solubility of water in our experimental system is close to our starting content of 2 wt. % according to the models of Papale et al. (2006) and Vetere et al. (2011). Either model implies that although some H_2O is transferred from the melt to the fluid phase on CO_2 saturation, most of the water remains in the melt. Carbonate assimilation will then progressively add more CO_2 to the fluid phase, meaning that in our experimental charges the final mixed H_2O-CO_2 vapour phase is strongly CO_2dominated.

The potential of CO_2 released by carbonate assimilation in the experimental charges can be assessed using an average amount of carbonate and shoshonitic melt of 6.8 and 29 mg, respectively. The complete break-down of carbonate during our experiments will liberate 2.99 mg of CO_2, which corresponds to 4.89 wt. % of CO_2 in the experimental charge as a whole (versus $\leq$ 2 wt. % H_2O). Therefore, the experimental approach presented here shows that CO_2

liberation during carbonate assimilation can be significant under crustal magma reservoir conditions and may be an important factor in promoting explosive behaviour at the VVS.

6. Implications of the Vesuvius volcanic system

Magma-carbonate interaction is a relevant process in the VVS and is characterised by: ***i)*** the abundance of high temperature skarn xenoliths in the erupted products (e.g., Fulignati et al. 1998, 2004, 2005; Del Moro et al. 2001), ***ii)*** crustally-derived CO_2 detected via the chemical and isotope composition of Vesuvius fumaroles (e.g., Iacono-Marziano et al. 2009), and ***iii)*** the $\delta^{18}O$ isotope composition of mafic VVS minerals that experienced interaction with sedimentary carbonate already at considerable depths (Dallai et al. 2011). Judging from our experiments, interaction between carbonate and Vesuvius shoshonite is indeed a viable and likely very fast process (minutes to hours). Moreover, we have shown how this process will progressively enrich the host melt in CaO and likely also MgO (from dolostone), while generating a CO_2-rich fluid phase. The experimental products show that CO_2 is generated directly at the melt-carbonate interface. In nature, this gas phase would form bubbles at crustal levels (Holloway and Blank 1994) and be transported upwards through the magma plumbing and conduit system. Therefore, CO_2 fluxes at the VVS are probably highly variable over different timescales, and CO_2 emissions measured in volcanic fumaroles at Vesuvius, that show a dominance of crustal over mantle-derived CO_2 (e.g., Iacono-Marziano et al. 2009), may be explained by the process modeled in our experiments. Conceivably, large quantities of CO_2 may be rapidly liberated during, e.g., renewed magma injection into shallow levels of the VVS reservoir system, where magma-carbonate interaction and carbonate assimilation have the potential to promote erratic explosive behaviour over short timescales (cf. Deegan et al. 2010, 2011; Freda et al. 2011). This implication would appear to be relevant to other volcanic systems as well, notably Merapi, Indonesia (Chadwick et al. 2007; Deegan et al. 2010), the Colli Albani, Italy (Freda et al. 2011), Popocatépetl, Mexico (Goff et al. 2001; Schaaf et al. 2005), and maybe even Yellowstone, USA (Werner and Brantley 2003), that like Vesuvius

are emplaced within some type of carbonate crust. We conclude that magma-carbonate interaction in the upper crust is likely a significant process operating beneath Vesuvius, but is variable in intensity. This interaction likely involves limestone and dolostone compositions and is not always easily quantified by conventional petrochemical indices (e.g., Sr-Ca relationships). Independently of the exact nature of the carbonate considered, our experiments demonstrate that magma-carbonate interaction can rapidly release considerable quantities of crustal CO_2 with potentially direct consequences on explosive versus effusive eruptive behaviour of the volcanic system.

Acknowledgements

We are grateful to L. Civetta for providing the starting materials. V. Misiti and A. Cavallo kindly helped during the experimental and EMPA work at INGV and G. Nowell kindly supported the micro drilling and strontium isotope analysis at Durham University. Discussion with S. Mollo, G. Orsi, C. Siebe, L. Dallai and T. Walter is much appreciated. We thank D. Baker and two anonymous referees for constructive reviews. We also thank the Swedish Science Foundation (VR), the Centre for Natural Disaster Science (CNDS), Uppsala University (UU), the Royal Swedish Academy of Science (KVA), and the Istituto Nazionale di Geofisica e Vulcanologia (INGV) for generous financial support of our work.

References

Auger E, Gasparini P, Virieux J, Zollo A (2001) Seismic evidence of an extended magmatic sill under Mt. Vesuvius. Science 294:1510-1512.

Ayuso RA, De Vivo B, Rolandi G, Seal II RR, Paone A (1998) Geochemical and isotopic (Nd-Pb-Sr-O) variations bearing on the genesis of volcanic rocks from Vesuvius, Italy. J Volcanol Geotherm Res 82:53-78.

Baker DR (1991) Interdiffusion of hydrous dacitic and rhyolitic melts and the efficacy of rhyolite contamination of dacitic enclaves. Contrib Mineral Petrol 106:462-473.

Baker DR, Freda C, Brooker RA, Scarlato P (2005) Volatile diffusion in silicate melts and its effects on melt inclusions. Ann Geophy 28 699-717.

Barberi F, Bizouard H, Clocchiatti R, Metrich N, Santacroce R, Sbrana A (1981) The Somma-Vesuvius magma chamber: A petrological and vulcanological approach. Bull Volcanol 44:295-315.

Berrino G, Corrado G, Riccardi U (1998) Sea gravity on the Gulf of Naples: a contribution to delineating the structural pattern of the Vesuvian área. J Volcanol Geotherm Res 82:139-150.

Behrens H, Misiti V, Freda C, Vetere F, Botcharnikov RE, Scarlato P (2009) Solubility of H_2O and CO_2 in ultrapotassic melts at 1200 and 1250 °C and pressure from 50 to 500 MPa. Am Mineral 94:105–120.

Blank JG, Brooker RA (1994) Experimental studies of carbon dioxide in silicate melts: solubility, speciation, and stable carbon isotope behaviour. In: Carroll M.R., Holloway J.R. (ed) Volatiles in magmas. Rev Mineral 20:157-186.

Blythe L, Misiti V, Masotta M, Taddeucci J, Freda C, Troll VR, Deegan FM, Jolis EM (2012) Viscosity controlled magma-carbonate interaction: a comparison of Mt. Vesuvius (Italy) and Mt. Merapi (Indonesia). Geophys Res Abstracts 14, EGU2012-4779-1

Botcharnikov R, Freise M, Holtz F, Behrens H (2005) Solubility of C-O-H mixtures in natural melts: new experimental data and implication range of recent models. Ann Geophys 48:633-646.

Brocchini D, Principe C, Castradori D, Laurenzi MA, Gorla L (2001) Quaternary evolution of the southern sector of the Campanian Plain and early Somma-Vesuvius activity: Insights from the Trecase 1 well. Mineral. Petrol. 73:67-91.

Chadwick JP, Troll VR, Ginibre C, Morgan D, Gertisser R, Waight TE, Davidson JP (2007) Carbonate assimilation at Merapi volcano, Java, Indonesia: Insights from crystal isotope stratigraphy. J Petrol 48:1793-1812.

Charlier BLA, Ginibre C, Morgan D, Nowell GM, Pearson DG, Davidson JP, Ottley CJ (2006) Methods for microsampling and high-precision analysis of strontium and rubidium at single crystal scale for petrological and geochronological applications. Chem Geol 232:114-133.

Civetta L, D'Antonio M, De Lorenzo S, Di RenzoV, Gasparini P (2004) Thermal and geochemical constraints on the 'deep' magmatic structure of Mt. Vesuvius. J Volcanol Geotherm Res 133:1-12.

Dallai L, Freda C, Gaeta M (2004) Oxygen isotope geochemistry of pyroclastic clinopyroxene monitors carbonate contributions to Roman-type ultrapotassic magmas. Contrib Mineral Petrol 148:247-263.

Civetta L, Galati R, Santacroce R (1991) Magma mixing and convective compositional layering within the Vesuvius magma chamber. Bull Volcanol 53:287-300.

Dallai L, Cioni R, Boschi C, D'Oriano C (2011) Carbonate-derived CO_2 purging magma at depth: influence on the eruptive activity of Somma-Vesuvius, Italy. Earth Planet Sci Lett 310:84-95.

Dallai L, Freda C, Gaeta M (2004) Oxygen isotope geochemistry of pyroclastic clinopyroxene monitors carbonate contributions to Roman-type ultrapotassic magmas. Contrib Mineral Petrol 148:247-263.

Dingwell DB (1996) Volcanic dilemma: flow or blow?. Science 273:1054-1055.

D'Antonio M, Civetta L, Orsi G, Pappalardo L, Piochi M, Carandente A, De Vita S, Di Vito MA, Isaia R, Southon J (1999) The present state of the magmatic system of the Campi Flegrei caldera based on the reconstruction of its behaviour in the past 12 ka. J Volcanol Geotherm Res 91:247–268.

De Campos CP, Dingwell DB, Perugini D, Civetta L, Fehr TK (2008) Heterogeneities in Magma Chambers: insights from the behavior of major and minor elements during mixing experiments with natural alkaline melts. Chem Geol 256:130–144.

Deegan FM, Troll VR, Freda C, Misiti V, Chadwick JP (2011) Fast and furious: crustal CO_2 release at Merapi volcano, Indonesia. Geol Today 27:57-58.

Deegan FM, Troll VR, Freda C, Misiti V, Chadwick JP, McLeod CL, Davidson JP (2010) Magma-carbonate interaction processes and associated CO_2 release at Merapi volcano, Indonesia: insights from experimental petrology. J Petrol 51:1027-1051.

Di Matteo V, Mangiacapra A, Dingwell DB, Orsi G (2006) Water solubility and speciation in shoshonitic and latitic composition from Campi Flegrei Caldera (Italy). Chemical Geology, 229:113-124.

Del Moro A, Fulignati P, Marianelli P, Sbrana A (2001) Magma contamination by direct wall rock interaction: constraints from xenoliths from the wall of carbonate-hosted magma chamber (Vesuvius 1944 eruption). J Volc Geotherm Res 112:15-24.

Del Pezzo E, Bianco F, De Siena L, Zollo A (2006) Small scale shallow attenuation structure at Mt. Vesuvius, Italy. Phys Earth Planet. Inter 157:257-268.

Di Renzo V, Di Vito MA, Arienzo I, Carandente A, Civetta L, D'Antonio M, Giordano F, Orsi G, Tonarini S (2007) Magmatic History of Somma-Vesuvius on the basis of new geochemical and isotopic data from a deep borehole (Camaldoli della Torre). J Petrol 48:753-784.

Dixon JE (1997) Degassing of alkali basalts. Am Mineral 82: 368-378.

Font L, Davidson JP, Pearson DG, Nowell GM, Jerram DA, Ottley CJ (2008) Sr and Pb isotope micro-analysis of plagioclase crystals from Skye lavas: an insight into open-system processes in a flood basalt province. J Petrol 49:1449-1471.

Freda C, Baker D, Ottolini L (2001) Reduction of water loss from gold-palladium capsules during piston cylinder experiments by use of pyrophyllite powder. Am Mineral 86:234-237.

Freda C, Gaeta M, Giaccio B, Marra F, Palladino DM, Scarlato P, Sottili G (2011) CO_2-driven large mafic explosive eruptions: the Pozzolane Rosse case study from the Colli Albani Volcanic District (Italy). Bull Volcanol 73:241-256.

557 Freda C, Gaeta M, Misiti V, Mollo S, Dolfi D, Scarlato P (2008) Magma-carbonate
558 interaction: An experimental study on ultrapotassic rocks from Alban Hills (Central Italy).
559 Lithos 101:397-415.
560
561 Freda C, Gaeta M, Palladino DM, Trigila R (1997) The Villa Senni Eruption (Alban
562 Hills, central Italy): the role of H_2O and CO_2 on the magma chamber evolution and on the
563 eruptive scenario J Volcanol Geotherm Res 78:103-120.
564
565 Fulignati P, Gioncada A, Sbrana A (1995) The magma chamber related hydrothermal
566 system of Vesuvius, first mineralogical and fluid inclusion data on hydrothermalized
567 subvolcanic and lavic samples from phreatomagmatic eruptions. Per Mineral 64:185-187.
568
569 Fulignati P, Marianelli P, Santacroce R, Sbrana A (2004) Probing the Vesuvius
570 magma chamber-host rock interface through xenoliths. Geol Mag 141:417-428.
571
572 Fulignati P, Marianelli P, Sbrana A (1998) New insights on the thermometamorphic-
573 metasomatic magma chamber shell of the 1944 eruption of Vesuvius. Acta Vulcanol 10:47-
574 54.
575
576 Fulignati P, Panichi C, Sbrana A, Caliro S, Gioncada A, Del Moro A (2005) Skarn
577 formation at the walls of the 79AD magma chamber of Vesuvius (Italy): minerological and
578 isotopic constraints. N Jb Miner Abh 181:53-66.
579
580 Gaeta M, Di Rocco T, Freda C (2009) Carbonate assimilation in open magmatic
581 systems: the role of melt-bearing skarns and cumulate forming processes. J Petrol 50:361-385.
582
583 Gilg HA, Lima A, Somma R, Belkin HE, De Vivo B, Ayuso RA (2001) Isotope
584 geochemistry and fluid inclusions study of skarns from Vesuvius. Mineral Petrol 73:145-176.
585
586 Ghiorso MS, Hirschmann MM, Sack RO (1994) New software models-
587 thermodynamics of magmatic systems. EOS Transactions, American Geophysical Union
588 75:574-576.
589
590 Goff F, Love SP, Warren RG, Counce D, Obenholzner J, Siebe C, Schmidt SC (2001)
591 Passive infrared remote sensing evidence for large, intermittent CO_2 emissions at Popcatépetl
592 volcano, Mexico. Chem Geol 177:133-156.
593
594 Holloway JR (1976) Fluids in the evolution of granitic magmas: consequences of
595 finite CO_2 solubility. Geol Soc Am Bull 87:1513-1518.
596
597 Holloway JR, Blank JG (1994) Application of experimental results to C–O–H species
598 in natural melts. In: Carroll M.R., Holloway J.R. (eds) Volatiles in magmas. Rev Mineral
599 30:187–230.
600
601 Iacono-Marziano G, Gaillard F, Pichavant M (2008) Limestone assimilation by
602 basaltic magmas: an experimental re-assessment and application to Italian volcanoes. Contrib
603 Mineral Petrol 155:719-738.
604
605 Iacono-Marziano G, Gaillard F, Scaillet B, Pichavant M, Chiodini G (2009) Role of
606 non-mantle CO_2 in the dynamics of volcano degassing: the Mount Vesuvius example.
607 Geology 37:319-322.

Iannace A, Capuano M, Galluccio L (2011) Dolomites and dolomites'' in Mesozoic platform carbonates of the Southern Apennines: Geometric distribution, petrography and geochemistry, Palaeogeogr Palaeoclimatol Palaeoecol 310:324-339.

Iezzi G, Mollo S, Ventura G, Cavallo A, Romano C (2008) Experimental solidification of anhydrous latitic and trachytic melts at different cooling rates: the role of nucleation kinetics. Chem Geol 253:91-101.

Lesher CE, Hervig RL, Tinker D (1996) Self diffusion of network formers (silicon and oxygen) in naturally occurring basaltic liquid. Geochim Cosmochim Acta 60:405-413.

Lesne P, Scaillet B, Pichavant M, Beny J-M (2010) The carbon dioxide solubility in alkali basalts: an experimental study. Contrib Mineral Petrol 162:133-151.

Liang Y, Richter FM, Davis, AM, Watson EB (1996) Diffusion in silicate melts I. Self diffusion in CaO-Al_2O_3-SiO_2 at 1500°C and 1 Gpa. Geochim Cosmochim Acta 60:4353-4367.

Metz P, Milke R, (2012) Mechanism and kinetics of forsterite formation in metamorphic siliceous dolomites: finding form a rock-sample experiment. Eur J Mineral 24:59-72.

Mollo S, Gaeta M, Freda C, Di Rocco T, Misiti V, Scarlato P (2010) Carbonate assimilation in magmas: a reappraisal based on experimental petrology. Lithos 114: 503-514.

Mollo S, Heap MJ, Iezzi G, Hess K-U, Scarlato P, Dingwell D (2012) Volcanic edifice weakening via decarbonation: a self-limiting processes?. Geophys Res Lett 39:L15307, doi:10.1029/2012GL052613.

Moore G, (2008) Interpreting H_2O and CO_2 contents in melt inclusions: constraints from solubility experiments and modeling. Rev. Mineral. Geochem. 69:333-361.

Orsi G, De Vita S, Di Vito M (1996) The restless, resurgent Campi Flegrei nested caldera(Italy): constraints on its evolution and configuration. J Volcanol Geotherm Res 74:179 -214.

Paone A (2006) The geochemical evolution of the Mt. Somma-Vesuvius volcano. Mineral Petrol 87:53-80.

Papale P, Moretti R, Barbato D (2006) The compositional dependence of the saturation surface of H_2O + CO_2 fluids in silicate melts. Chem Geol 229:78-95.

Peccerillo A (1999) Multiple metasomatism in central-southern Italy: Geochemical effects, timing and geodynamic implications. Geology, 27:315-318.

Peccerillo A (2005) Plio-Quaternary volcanism in Italy. Petrology, Geochemistry, Geodynamics. Eds: Springer Berlin Heidelber New York, pp-133-135.

Perugini D, Petrelli M, Poli G (2006) Diffusive fractionation of trace elements by chaotic mixing of magmas. Earth Planet. Sci. Lett 243:669-680.

659 Perugini D, De Campos CP, Dingwell DB, Petrelli M, Poli G (2008) Trace element
660 mobility during magma mixing: Preliminary experimental results. Chem Geol 256:146-157.
661
662
663 Piochi M, Ayuso RA, De Vivo B, Somma R (2006) Crustal contamination and crystal
664 entrapment during polybaric magma evolution at Mt. Somma-Vesuvius volcano, Italy:
665 geochemical and Sr isotope evidence. Lithos, 86:303-329.
666
667 Rittmann A (1933) Evolution and differentiation des Somma-Vesuvius-magmas. Zs.
668 Vulkanologie 15:8-94.
669
670 Rolandi G, Munno R, Postiglione I (2004) The A.D. 472 eruption of the Somma
671 volcano. J Volcanol Geotherm Res 129:291-319.
672
673 Schaaf P, Stimac J, Siebe C, Macias JL (2005) Geochemical evidence for mantle
674 origin and crustal processes in volcanic rocks from Popocatépetl and surrounding
675 monogenetic volcanoes, Central Mexico. J Petro 46:1243-1282.
676
677 Somma R, Ayuso RA, De Vivo B, Rolandi G (2001) Major, trace element and isotope
678 geochemistry (Sr-Nd-Pb) of interplinian magmas from Mt. Somma-Vesuvius (Southern Italy).
679 Mineral Petrol 73:121-143.
680
681 Thirlwall MF (1991) Long-term reproducibility of multicollector Sr an Nd isotope
682 ratio analysis. Chem Geol 94:85-104.
683
684 Troll VR, Deegan FM, Jolis EM, Harris C, Chadwick JP, Gertisser R, Schwarzkopf
685 LM, Borisova AY, Bindeman IN, Sumarti S, Preece K (2012b) Magmatic differentiation
686 processes at Merapi Volcano: inclusions petrology and oxygen isotopes. J Volcanol Res, in
687 press. Doi:10.16/j.jvolgeores.2012.11001.

688 Troll, VR, Hilton DR, Jolis EM, Chadwick JP, Blythe LS, Deegan F M, Schwarzkopf
689 LM, Zimmer M (2012a) Crustal CO_2 liberation during the 2006 eruption and earthquake
690 events at Merapi volcano, Indonesia. Geophys Res Lett 39:L11302,
691 doi:10.1029/2012GL051307.

692 Turi B, Taylor HPJr (1976) Oxygen isotope studies of potassic volcanic rocks of the
693 Roman Province, Central Italy. Contrib Mineral Petrol 55:1-31.
694
695 Vetere F, Botcharnikov RE, Holtz F, Behrens H, De Rosa R (2011) Solubility of H_2O
696 and CO_2 in shoshonitic melts at 1250°C and pressures from 50 to 400 MPa: implications from
697 Campi Flegrei magmatic systems. J Volcanol Geotherm Res 202:251-261.
698
699 Watson BE (1982) Basalt contamination by continental crust: some experiments and
700 models. Contrib Mineral Petrol 80:73-87.
701
702 Watson EB, Jurewicz SR (1984) Behavior of alkalies diffusive of granitic xenoliths
703 with basaltic magma. J Geol 92:121-131.
704 Watson BE, Sneeringer MA, Ross A (1982) Diffusion of dissolved carbonate in
705 magmas: experimental results and applications. Earth Planet Sci Lett 61:356-358.
706

Werner C, Brantley S (2003) CO_2 emissions from the Yellowstone volcanic system. Geochem Geophys Geosyst 4, doi: 10.1029/2002GC000473.

Zhang Y (2010) Diffusion in minerals and melts: theoretical background. In Zhang Y and Cherniak DJ (eds) Rev Mineral Geochem v. 72, pp 5-59.

Zhang Y (1993) A modified effective binary diffusion model. J. Geophys Res 98:11901-11920.

Zhang Y, Stolper EM (1991) Water diffusion in a basaltic melt. Nature 351:306-309.

Zollo A, Gasparini P, Virieux J, Biella G, Boschi E, Capuano P, De Franco R, Dell'Aversana P, De Matteis R, De Natale G, Iannaccone G, Guerra I, Le Meur H, Mirabile L (1998) An image of Mt. Vesuvius obteined by 2D seismic tomography. J Volcanol Geotherm Res 82:161-173.

Zollo A, Gasparini P, Virieux J, Le Meur H, De Natale G, Biella G, Boschi E, Capuano P, De Franco R, Dell'Aversana P, De Matteis R, Guerra I, Iannaccone G, Mirabile, L, Vilardo G (1996) Seimic Evidence for a Low-Velocity Zone in the Upper Crust Beneath Mount Vesuvuis. Science 274:592-594.

Zollo A, Marzocchi W, Capuano P, Lomax A, Iannaccone G (2002) Space and time behavior of seismic activity at Mt.Vesuvius volcano, Southern Italy. Bull Seismol Soc Am 92: 625-640.

Figure Captions

Figure 1. BSE images of experimental products with increasing experimental durations (t_d = 0 to 300 s): limestone-bearing experiments (**a**, **b**, **c** and **d)** and dolostone-bearing experiments in (**e**, **f**, **g**, and **h)**. Experiments show: *i*) a solid phase, i.e., calcite crystallite domains – marked with a broken white line in images **a**, **b** and **c** - and olivine and pyroxene crystals in images **f**, **g** and **h**; *ii*) a melt phase, i.e., Ca-normal, and Ca-rich and Ca-Mg-rich glasses; and *iii*) a vapour phase, preserved as bubbles. Note the contrasting brightness between Ca-rich and Ca-Mg-rich, and Ca-normal glasses in the images (light and dark colour, respectively).

Figure 2. BSE images showing dendritic micro-crystals of calcite in limestone-bearing experiments at t_d = 60 and 90 s (**a**, **b**), and clinopyroxene and olivine crystals from the dolostone-bearing experiments at t_d = 90 and 300 s (**c**, **d**). Abbreviations: Ol: olivine and Cpx: clinopyroxene.

Figure 3. Ternary diagrams of mineral compositions in dolostone-bearing experiments. Composition of pyroxenes in the $CaSiO_3$ – $MgSiO_3$ – $FeSiO_3$ system (**a**)**.** Composition of olivines in the Ca_2SiO_4– Mg_2SiO_4 - Fe_2SiO_4 system (small inset triangle). The bottom left hand corner of the small triangle is shown in large (**b**).

Figure 4. Representative microprobe chemical traverses in 0, 60, 90 and 300 s limestone-bearing experiments (**a** to **d**). The white lines in the images show the EMPA traverses (A to A') that correspond to the plots on the right. The Ca-normal and Ca-rich glasses are dark and pale grey in colour, respectively, and are separated by a dashed white line. The contamination front (CF) is the interfacial region between Ca-normal and Ca-rich domains. This area corresponds to a physico-chemical mixing and diffusion interface between the glass domains. Note that the width of the CF (delimited by vertical dashed lines on the right graphs) differs in the various experimental runs.

Figure 5. Representative microprobe chemical traverses in 0, 60, 90 and 300 s dolostone-bearing experiments (**a** to **d**). The solid white lines drawn on the images show the EMPA traverses (A to A') corresponding to the plots on the right. The contact between contaminated and uncontaminated melts is highlighted with white dashed lines (CF). See also **Fig 4**.

Figure 6. $^{87}Sr/^{86}Sr$ and CaO wt % profiles in the 60 s (**a**) and the 90 s (**b**) limestone-bearing experiments. The solid lines in the BSE images show different traverses in a single experiment (from A to A'). Drilled areas are numbered and highlighted in white on the BSE images. The right side of images for **a**) and **b**) correspond to the CaO wt. % from EMPA traverse (upper diagram) and the $^{87}Sr/^{86}Sr$ isotope ratios of the drilled areas (lower diagram). The height of the rectangles in the $^{87}Sr/^{86}Sr$ diagram represents the ±2SE analytical uncertainty and their locations relative to the EMPA traverse data are approximate (see **Table 4**). The dark and pale shaded areas represent the glass domains observed in our experiments and the blue and green horizontal dashed lines are the CaO wt. % and $^{87}Sr/^{86}Sr$ ratios of the starting materials.

Figure 7. $^{87}Sr/^{86}Sr$ and CaO wt. % profiles in the dolostone-bearing experiments. **a)** BSE image of the 60 s experiment and **b**), **c**) and **d**) show the 90 s experiment. The white lines in the images show different traverses in a single experiment (A to A'). The diagrams on the right side illustrate CaO wt. % (upper diagram) and $^{87}Sr/^{86}Sr$ (lower diagram) for the different traverses and drill holes, respectively. The height of the rectangles in the $^{87}Sr/^{86}Sr$ diagram includes the ±2SE analytical uncertainty and their locations of the drill holes relative to the EMPA traverses are approximate. The traverse in panel **b)** extends beyond the BSE image. Abbreviations as in **Fig 6**.

Figure 8. Compositional summary diagram of all limestone-bearing experiments. Binary mixing trajectory between shoshonite and limestone is illustrated. The experiments are represented by: triangles for t_d = 0 s (n = 17); diamonds for t_d = 60 s (n = 27); squares for t_d =

90 s (n = 21); circles for t_d = 300 s (n = 11). The glass domains and the interface region are given as: dark grey = Ca-rich, pale grey = Ca-normal, and white = contamination front. The maximum degree of chemical mixing of ambient melt with carbonate derived CaO is reached at t_d = 90s and equates to about 60 %. Note that at t_d = 300 s (highlighted with a red line), the system has progressively homogenised (less than 25 % carbonate derived CaO in mixture). The small displacement of CaO and SiO_2 above the linear binary mixing trajectory reflects fluctuations of these elements as a consequence of transport through convection and interdiffusion between the experimental melts (see text for details and **Online Resource 1 Fig OR1**).

Figure 9. Compositional summary diagram of all dolostone-bearing experiments. Binary mixing trajectory between shoshonite and dolostone is represented. The symbols for each experiment and the colours of glass domains are the same as in **Fig 8**. The total number of data points in each experiment is: n = 12 for t_d = 0 s; n = 80 for t_d = 60 s; n = 137 for t_d = 90 s; n = 23 for t_d = 300 s. For these experiments, the system reached its maximum degree of mixing at t_d = 60 to 90 s. For t_d = 300 s (highlighted with a red line) the glass has again adopted a more homogenous composition. The deviations from the binary mixing trajectory is likely a coupled consequence of melt transport, as in the limestone-bearing experiments, but was affected by simultaneous crystal growth and associated Mg removal from the melt (see also **Online Resource 1 Fig OR2**).

Figure 10. a) $^{87}Sr/^{86}Sr$ values for our experimental glasses in comparison to VVS shoshonite magma compositions, Vesuvius skarn xenoliths, and local carbonate crust. The Ca-normal glass is within the range of the natural shoshonite magmas, whereas the contaminated glass is displaced towards crustal values and overlaps with the range of skarns reported from the VVS. **b**) $^{87}Sr/^{86}Sr$ vs. Sr (ppm) diagram illustrates possible binary mixing relationships. Triangles and circles represent the limestone-bearing experiments for t_d at 60 and 90 s, respectively, whereas squares and diamonds are the dolostone-bearing experimental products for the same

experimental durations. The mixing trajectories A-C_1 and A-C_2 define the mixing space between the shoshonite end-member (A) and the high $^{87}Sr/^{86}Sr$ and high Sr concentrations reported from some parts of the nearby carbonate crust. The mixing trajectories A-C_2, A-C_3, A-C_4 and A-C_5 form the mixing space between shoshonite (A) and the low $^{87}Sr/^{86}Sr$ and low-Sr ppm carbonates reported from the Campanian region (see text for details). The majority of the drilled experimental glass compositions fall within the low Sr-carbonate mixing space (mixing curves A-C_2 to A-C_5), implying mixtures of between 55 and 75% carbonate-derived $^{87}Sr/^{86}Sr$ relative to shoshonite. Literature data from: Civetta et al. (1991); Di Renzo et al. (2007); Del Moro et al. (2009); Piochi et al. (2006); Iannace et al. (2011).

Table 1: *Starting material composition*

	Hydrous glass [(a)]	1σ (9) [(b)]	Limestone CaVe1 Procida[(c)]	Dolostone CaVe3 Procida[(d)]
SiO_2	49.85	0.21	0.02	0.02
TiO_2	1.03	0.08	-	-
Al_2O_3	15.95	0.67	-	-
FeO_t[(e)]	7.98	0.25	0.01	0.0
MnO	0.14	0.02	0.01	0.01
MgO	6.03	0.33	0.79	21.01
CaO	9.98	0.29	54.99	31.34
Na_2O	2.35	0.07	-	-
K_2O	4.01	0.19	-	-
P_2O_5	0.70	0.09	0.02	0.0
CO_2	-	-	44.11*	47.59*
H_2O	2		-	-
Total	100.02		100.00	100.00
Sr	735†		299††	89††
$^{87}Sr/^{86}Sr$†††	0.706661 ±8		0.7075 ±1	0.7072 ±1

[(a)] Hydrous glass synthesised from natural powdered rock at T = 1250 ºC and 0.5 GPa.
[(b)] 1σ standard deviation; the number in parenthesis represents the number of analyses.
[(c)] Lower Cretaceous limestone from Procida Formation.
[(d)] Triassic dolostone from Procida Formation.
[(a, c, d)] Major elements composition of the starting material were determined by electron-microprobe at INGV and given in wt. %.
[(e)] Total iron is given as FeOt.
*Fraction of CO_2 in the fluid phase was calculated assuming wt. % $CaCO_3$ in the samples as equivalent to 100 wt. % minus all other element oxides.
† Strontium content for shoshonitic melt: Di Renzo et al. (2007).
†† Limestone and dolostone Sr contents were determined by ICP-emission spectrometry at Acmelabs (Vancouver, Canada) and are given in ppm.
††† Strontium isotopes for: shoshonitic melt: Di Renzo et al. (2007); and for limestone and dolostone: Piochi et al. (2006) and Iannace et al. (2011).

Table 2: *Experimental Conditions*

Run #	Experimental time t_d (s)	Pressure (GPa)*	Temperature (ºC)*	Limestone (mg)	Dolostone (mg)	Hydrous glass ~ 2 wt. % H_2O (mg)
PC443-V5	0	0.5	1200	6.1	-	29.6
PC448-V9	60	0.5	1200	8.2	-	33.3
PC442-V3	60	0.5	1200	6.3	-	28.8
PC441-V1	90	0.5	1200	6.8	-	24.2
PC-445 V7	300	0.5	1200	7.2	-	26.0
PC443-V6	0	0.5	1200	-	6.0	30.0
PC448-V10	60	0.5	1200	-	7.7	34.2
PC442-V4	60	0.5	1200	-	7.0	29.6
PC441-V2	90	0.5	1200	-	6.0	30.0
PC445-V8	300	0.5	1200	-	7.1	26.4

*Pressure and temperature uncertainties are ± 0.02 GPa and ± 5 °C, respectively.

Table 3: *Representative electron microprobe chemical analyses*

Experimental run # *PC443-V5 Limestone-bearing*																	
Traverse 1																	
	Ca-normal glass			*Contamination Front (CF)*		*Ca-rich glass*				*Contamination Front (CF)*					*Ca-normal glass*		
SiO_2	50.3	49.7	49.8	49.2	42.2	32.3	29.8	30.4	35.3	41.0	39.2	39.3	42.6	48.5	49.7	49.3	50.1
TiO_2	1.0	1.0	1.0	1.0	0.7	0.7	0.7	0.7	0.7	0.8	0.8	0.9	0.9	1.0	1.0	1.0	0.9
Al_2O_3	15.6	15.5	15.3	15.2	13.2	9.6	9.1	9.7	11.3	12.8	12.2	12.5	13.3	15.2	15.3	15.9	16.2
FeO	6.6	6.5	6.1	5.6	4.8	4.5	4.8	4.9	4.7	5.7	6.1	6.1	6.4	5.9	7.2	7.0	7.1
MnO	0.1	0.1	0.2	0.1	0.1	0.1	0.1	0.1	0.1	0.1	0.1	0.1	0.1	0.1	0.1	0.1	0.1
MgO	5.5	5.5	5.3	4.9	4.3	4.4	3.8	3.5	4.1	5.0	5.4	5.2	5.3	4.8	5.7	5.6	5.7
CaO	9.1	9.3	10.2	11.7	22.2	30.9	31.5	30.2	29.3	21.6	23.8	23.7	20.9	13.0	9.6	9.1	9.1
Na_2O	3.0	2.9	2.9	2.6	1.7	1.3	1.1	0.9	1.1	1.5	1.3	1.4	1.5	2.2	2.6	2.5	2.6
K_2O	5.3	5.4	5.8	5.7	3.1	1.8	1.5	1.4	2.1	3.1	2.4	2.2	2.3	4.2	4.4	4.4	4.2
P_2O_5	0.6	0.7	0.6	0.6	0.4	0.5	0.5	0.4	0.3	0.6	0.5	0.4	0.5	0.7	0.6	0.6	0.6
SrO	0.1	0.2	0.1	0.1	0.0	0.0	0.1	0.1	0.0	0.0	0.1	0.1	0.1	0.1	0.1	0.1	0.0
BaO	0.1	0.1	0.2	0.1	0.0	0.0	0.1	0.0	0.1	0.1	0.2	0.1	0.1	0.3	0.2	0.1	0.1
Total*	97.3	96.9	97.5	96.8	92.7	86.1	83.0	82.5	89.1	92.4	92.1	92.0	93.9	95.7	96.5	95.8	96.8

Table 3 : *Continued*

Experimental run # *PC442-V4 Dolostone-bearing*																	
	Traverse 1										Traverse 2						
	Ca-Mg-normal glass					*Contamination front (CF)*			*Ca-Mg-rich glass*		*Contamination front (CF)*						
SiO_2	48.9	48.8	49.0	48.7	48.6	44.1	40.9	41.6	38.5	37.0	45.1	47.9	46.5	43.9	47.0	46.6	
Al_2O_3	1.1	0.9	0.9	1.0	0.9	1.0	1.1	0.7	0.8	0.7	1.0	1.0	0.9	1.0	1.0	0.9	
TiO_2	16.7	16.6	16.6	16.3	16.4	14.7	13.8	14.0	12.7	12.1	15.4	16.4	15.8	15.8	16.2	16.3	
FeO	6.5	6.3	6.6	6.2	6.1	6.6	6.9	6.1	5.7	5.4	5.7	5.3	5.5	5.7	5.5	5.5	
MnO	0.1	0.1	0.1	0.1	0.1	0.1	0.2	0.1	0.1	0.1	0.1	0.1	0.1	0.1	0.1	0.1	
MgO	5.8	5.7	5.7	5.8	5.8	7.8	8.7	8.4	9.2	9.0	7.1	5.5	7.2	7.8	6.6	6.7	
CaO	9.1	9.2	9.1	9.4	10.2	14.4	16.6	17.1	19.9	20.8	13.4	10.1	12.6	14.9	10.5	11.2	
Na_2O	3.0	2.9	3.1	3.1	2.9	2.2	1.9	1.9	1.6	2.4	2.4	2.9	2.6	2.3	3.0	3.0	
K_2O	3.9	4.0	4.0	4.2	4.1	2.6	2.2	2.6	2.1	2.3	3.7	4.9	3.6	3.0	4.3	4.2	
P_2O_5	0.6	0.5	0.6	0.6	0.7	0.6	0.6	0.6	0.6	0.5	0.5	0.7	0.5	0.6	0.6	0.6	
BaO	0.1	0.1	0.1	0.1	0.1	0.1	0.1	0.1	0.0	0.1	0.0	0.1	0.0	0.2	0.1	0.1	
SrO	0.2	0.1	0.2	0.0	0.1	0.1	0.2	0.2	0.0	0.1	0.3	0.3	0.2	0.1	0.1	0.1	
Total*	96.1	95.3	96.0	95.4	95.9	94.2	93.1	93.4	91.3	90.4	94.8	95.2	95.7	95.5	95.0	95.5	

Note: analyses shown are from the experimental glass regions: Ca-normal, Ca-rich and contamination front (CF).

*The low totals obtained are due to one of the following reasons: *a)* microbubbles (cf. Deegan et al., 2010), *b)* increased CO_2 solubility in alkaline and ultrapotassic melts in general (cf. Behrens et al., 2009) or *c)* increased CO_2 solubility in our Ca-rich experimental melt (Moore, 2008).

Limestone-bearing

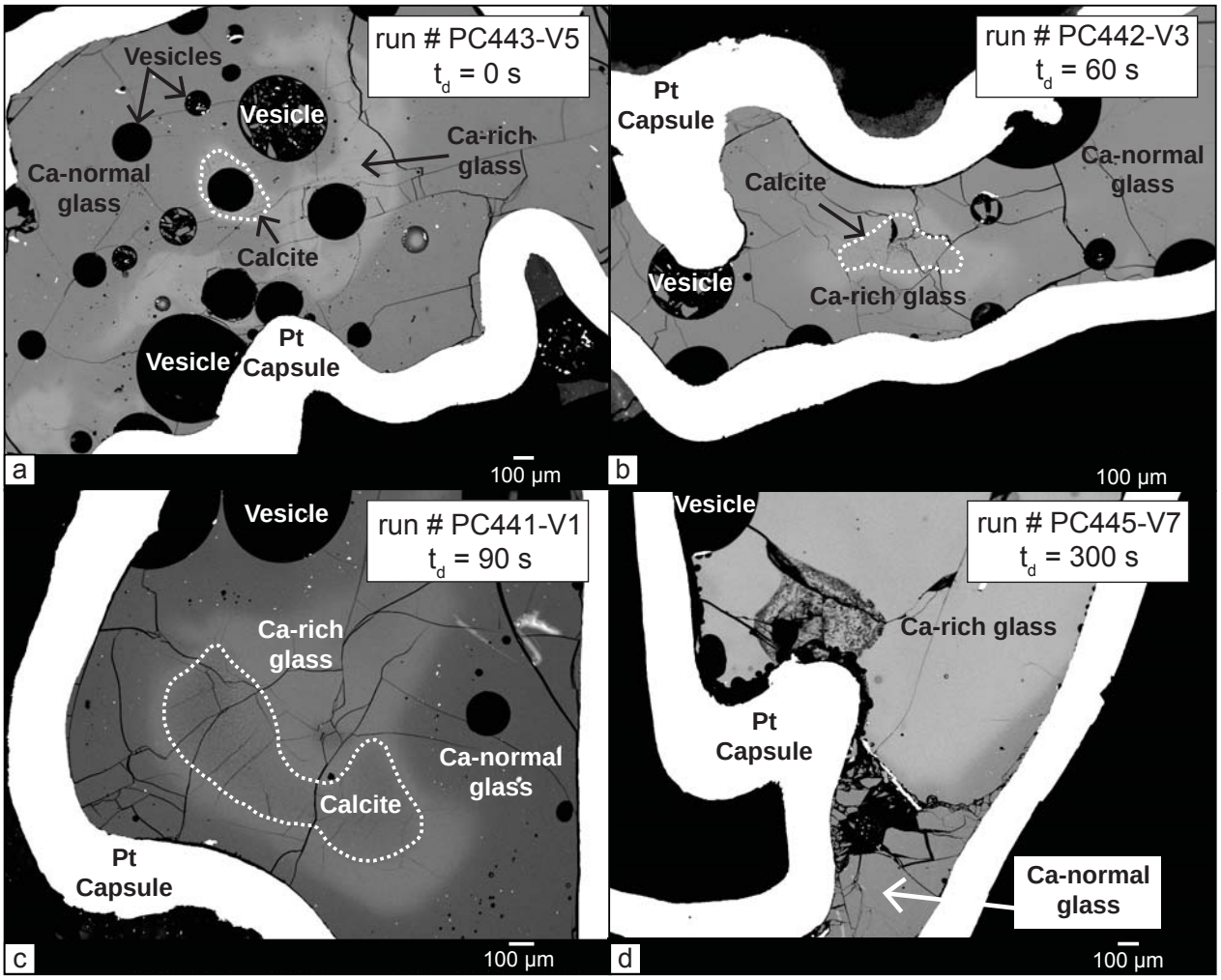

Dolostone-bearing

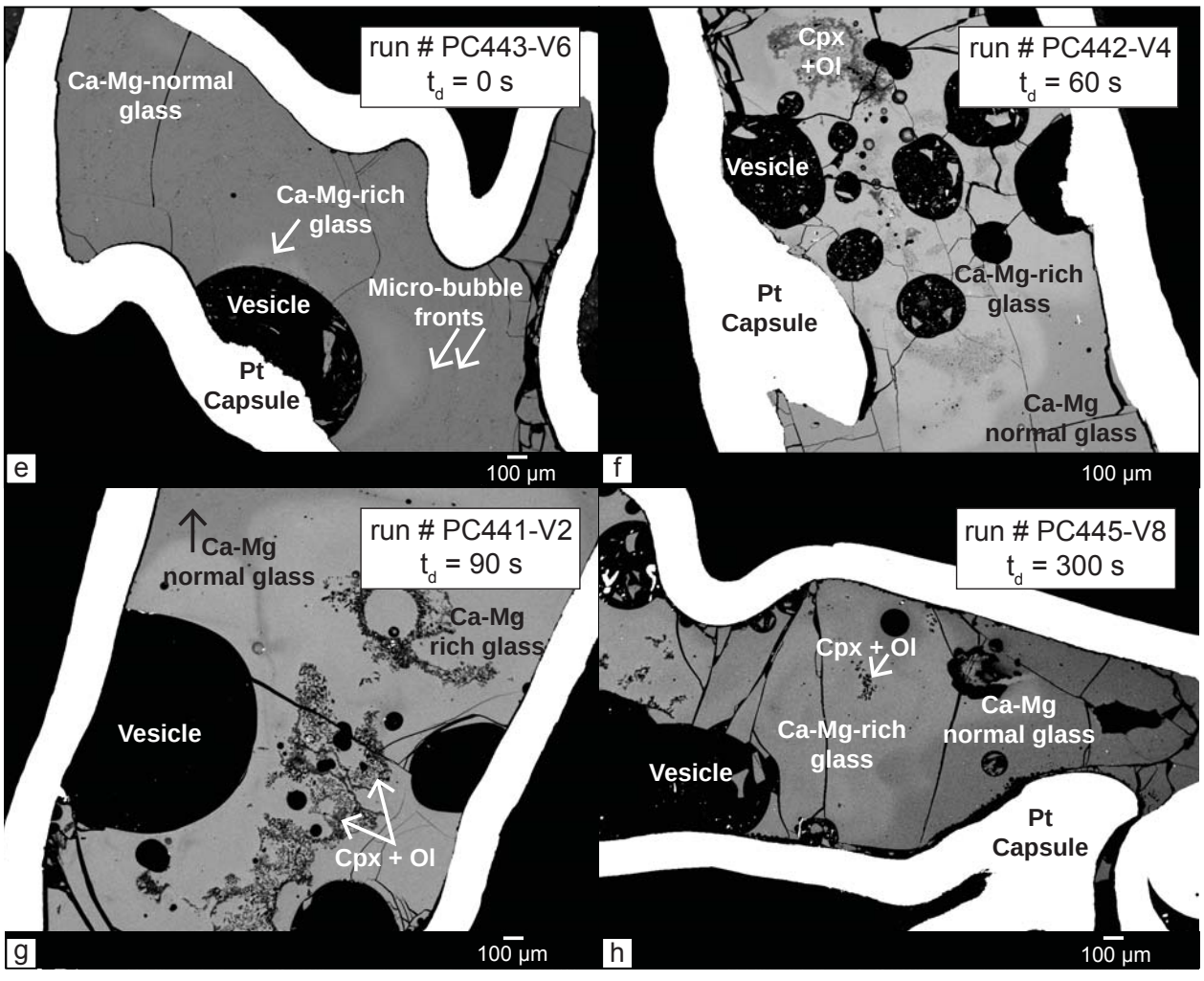

Figure 1

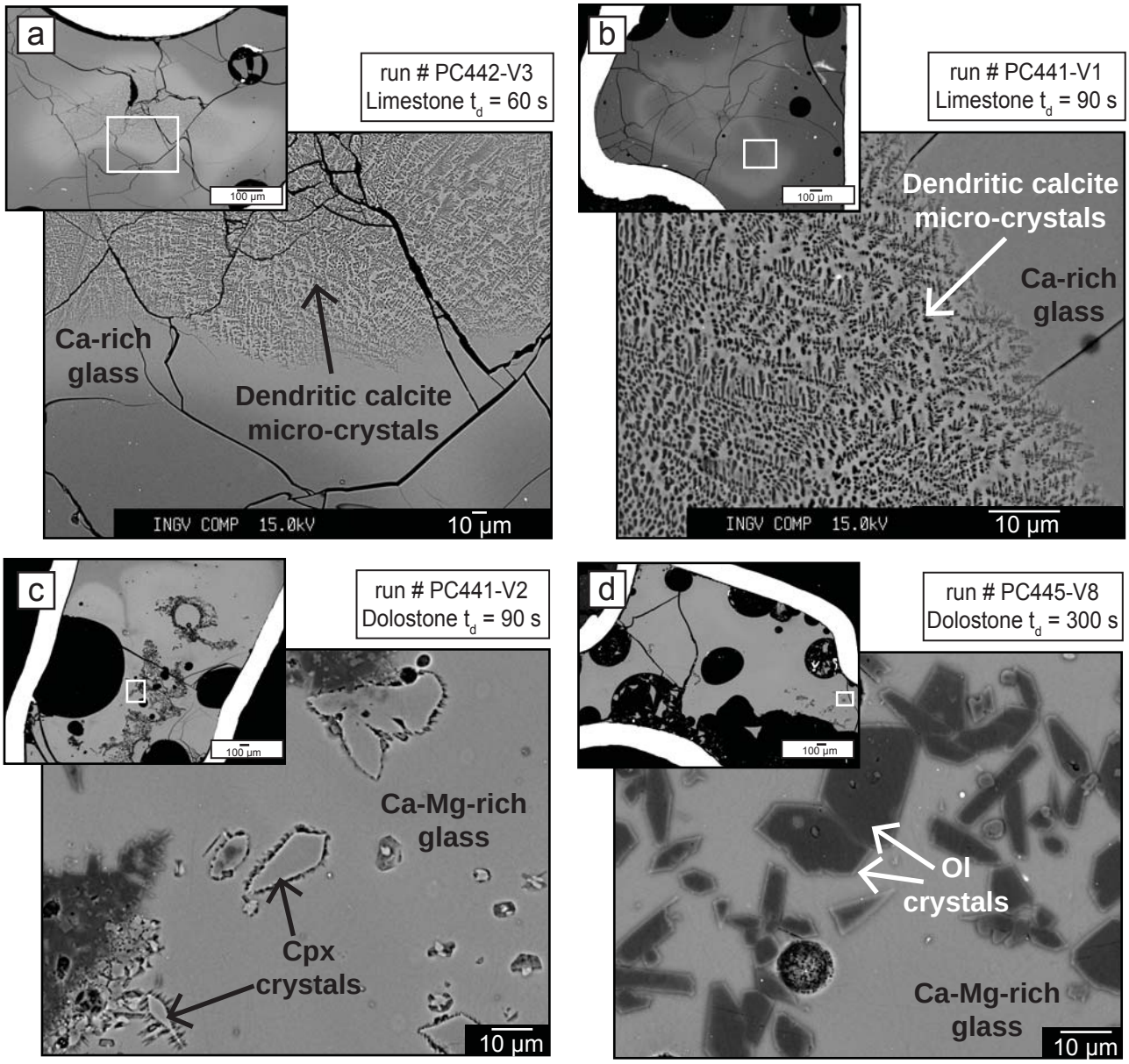
a
run # PC442-V3
Limestone t_d = 60 s
Ca-rich glass
Dendritic calcite micro-crystals
INGV COMP 15.0kV
10 µm
b
run # PC441-V1
Limestone t_d = 90 s
Dendritic calcite micro-crystals
Ca-rich glass
INGV COMP 15.0kV
10 µm
c
run # PC441-V2
Dolostone t_d = 90 s
Ca-Mg-rich glass
Cpx crystals
10 µm
d
run # PC445-V8
Dolostone t_d = 300 s
Ol crystals
Ca-Mg-rich glass
10 µm

Figure 2

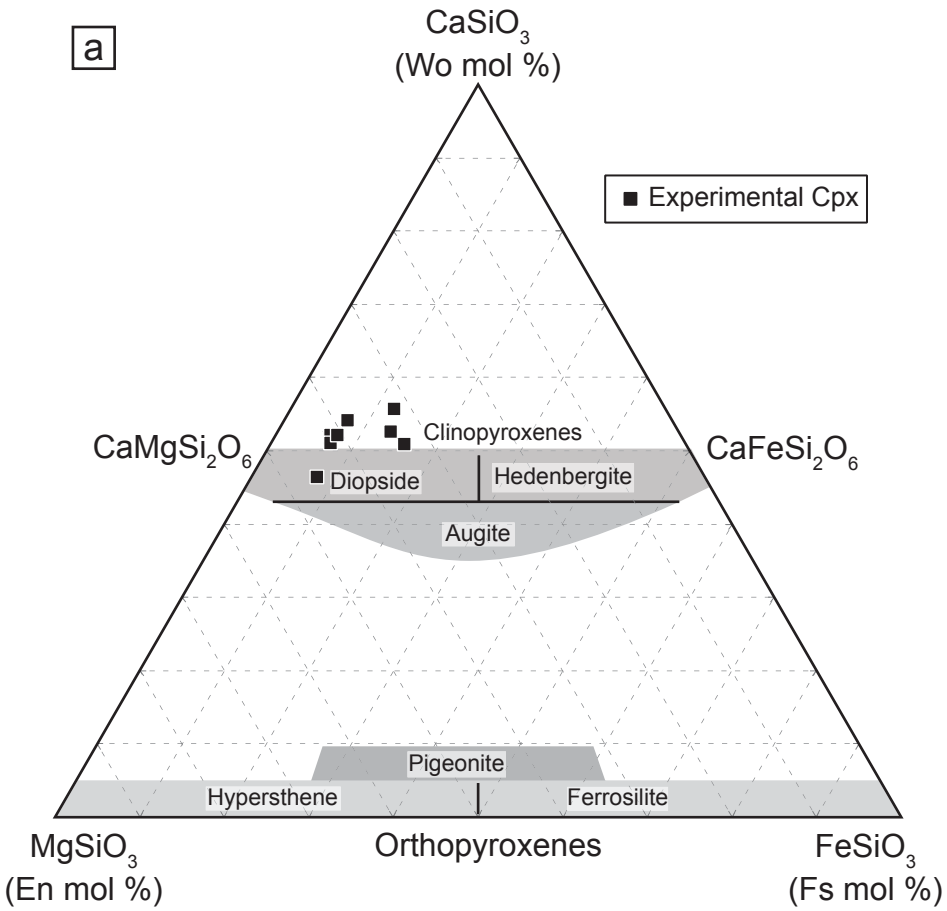
a
CaSiO3
(Wo mol %)
Experimental Cpx
CaMgSi2O6
CaFeSi2O6
Clinopyroxenes
Diopside
Hedenbergite
Augite
Pigeonite
Hypersthene
Ferrosilite
MgSiO3
(En mol %)
Orthopyroxenes
FeSiO3
(Fs mol %)

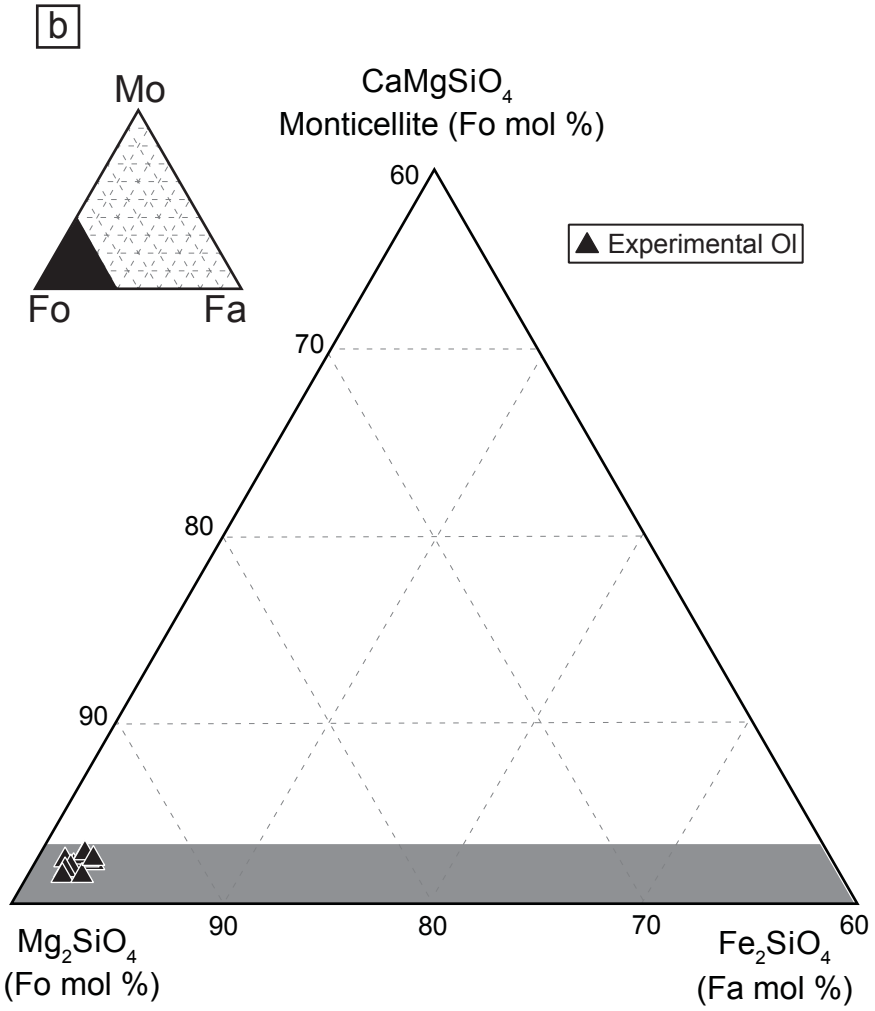
b
Mo
Fo
Fa
CaMgSiO4
Monticellite (Fo mol %)
Experimental Ol
60
70
80
90
90
80
70
60
Mg2SiO4
(Fo mol %)
Fe2SiO4
(Fa mol %)

Figure 3

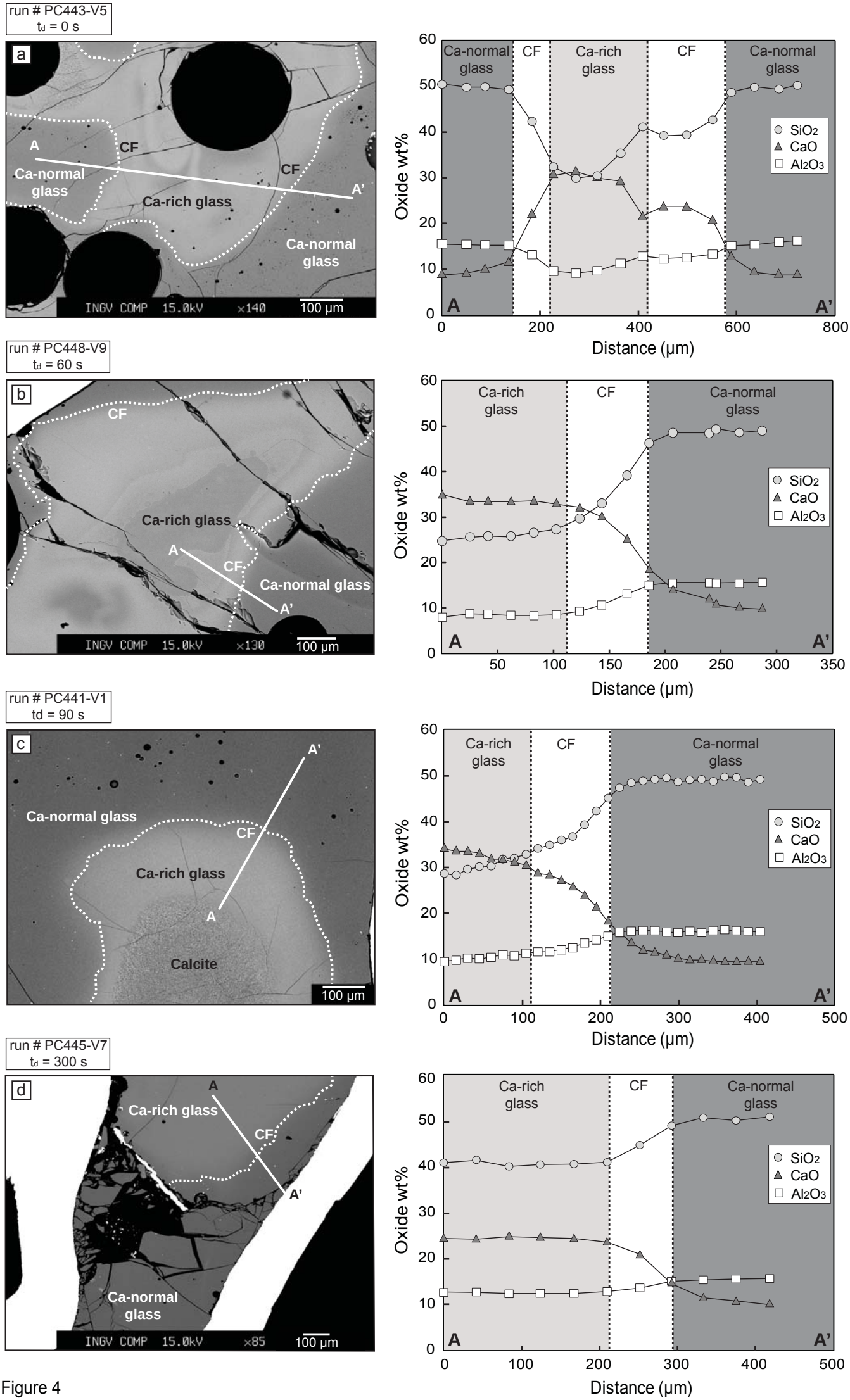
run # PC443-V5
td = 0 s
a
A
CF
Ca-normal glass
CF
A'
Ca-rich glass
Ca-normal glass
INGV COMP 15.0kV ×140 100 µm
Ca-normal glass
CF
Ca-rich glass
CF
Ca-normal glass
SiO2
CaO
Al2O3
Oxide wt%
Distance (µm)
run # PC448-V9
td = 60 s
b
CF
Ca-rich glass
A
CF
Ca-normal glass
A'
INGV COMP 15.0kV ×130 100 µm
Ca-rich glass
CF
Ca-normal glass
run # PC441-V1
td = 90 s
c
A'
Ca-normal glass
CF
Ca-rich glass
A
Calcite
100 µm
Ca-rich glass
CF
Ca-normal glass
run # PC445-V7
td = 300 s
d
A
Ca-rich glass
CF
A'
Ca-normal glass
INGV COMP 15.0kV ×85 100 µm
Ca-rich glass
CF
Ca-normal glass

Figure 4

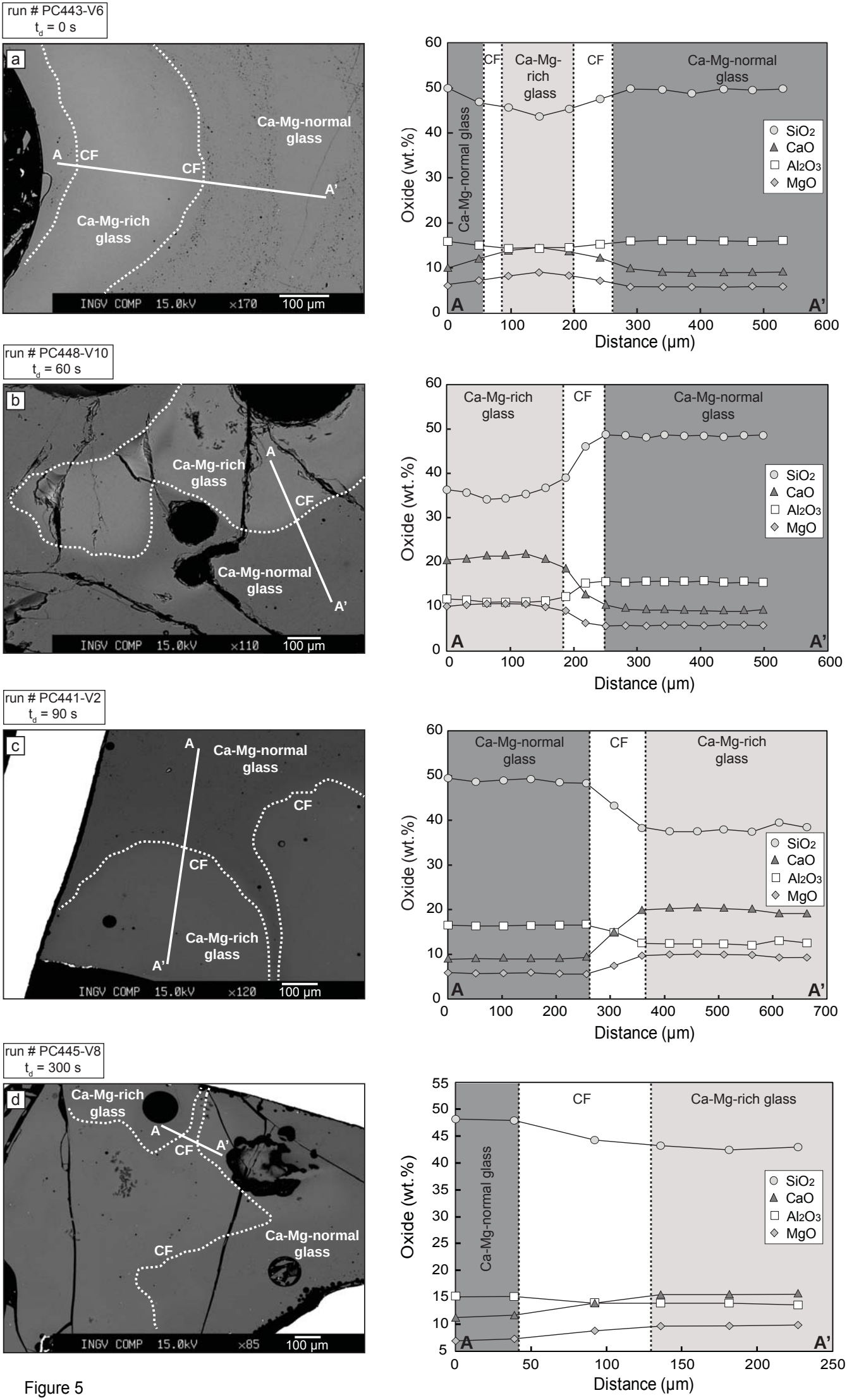
run # PC443-V6
t_d = 0 s
a
Ca-Mg-normal glass
A
CF
CF
A'
Ca-Mg-rich glass
INGV COMP 15.0kV ×170 100 µm
Ca-Mg-normal glass
CF
Ca-Mg-rich glass
CF
Ca-Mg-normal glass
Oxide (wt.%)
Distance (µm)
SiO2
CaO
Al2O3
MgO
A
A'
run # PC448-V10
t_d = 60 s
b
Ca-Mg-rich glass
A
CF
Ca-Mg-normal glass
A'
INGV COMP 15.0kV ×110 100 µm
Ca-Mg-rich glass
CF
Ca-Mg-normal glass
Oxide (wt.%)
Distance (µm)
SiO2
CaO
Al2O3
MgO
A
A'
run # PC441-V2
t_d = 90 s
c
A
Ca-Mg-normal glass
CF
CF
Ca-Mg-rich glass
A'
INGV COMP 15.0kV ×120 100 µm
Ca-Mg-normal glass
CF
Ca-Mg-rich glass
Oxide (wt.%)
Distance (µm)
SiO2
CaO
Al2O3
MgO
A
A'
run # PC445-V8
t_d = 300 s
d
Ca-Mg-rich glass
A
CF
A'
CF
Ca-Mg-normal glass
INGV COMP 15.0kV ×85 100 µm
CF
Ca-Mg-rich glass
Ca-Mg-normal glass
Oxide (wt.%)
Distance (µm)
SiO2
CaO
Al2O3
MgO
A
A'

Figure 5

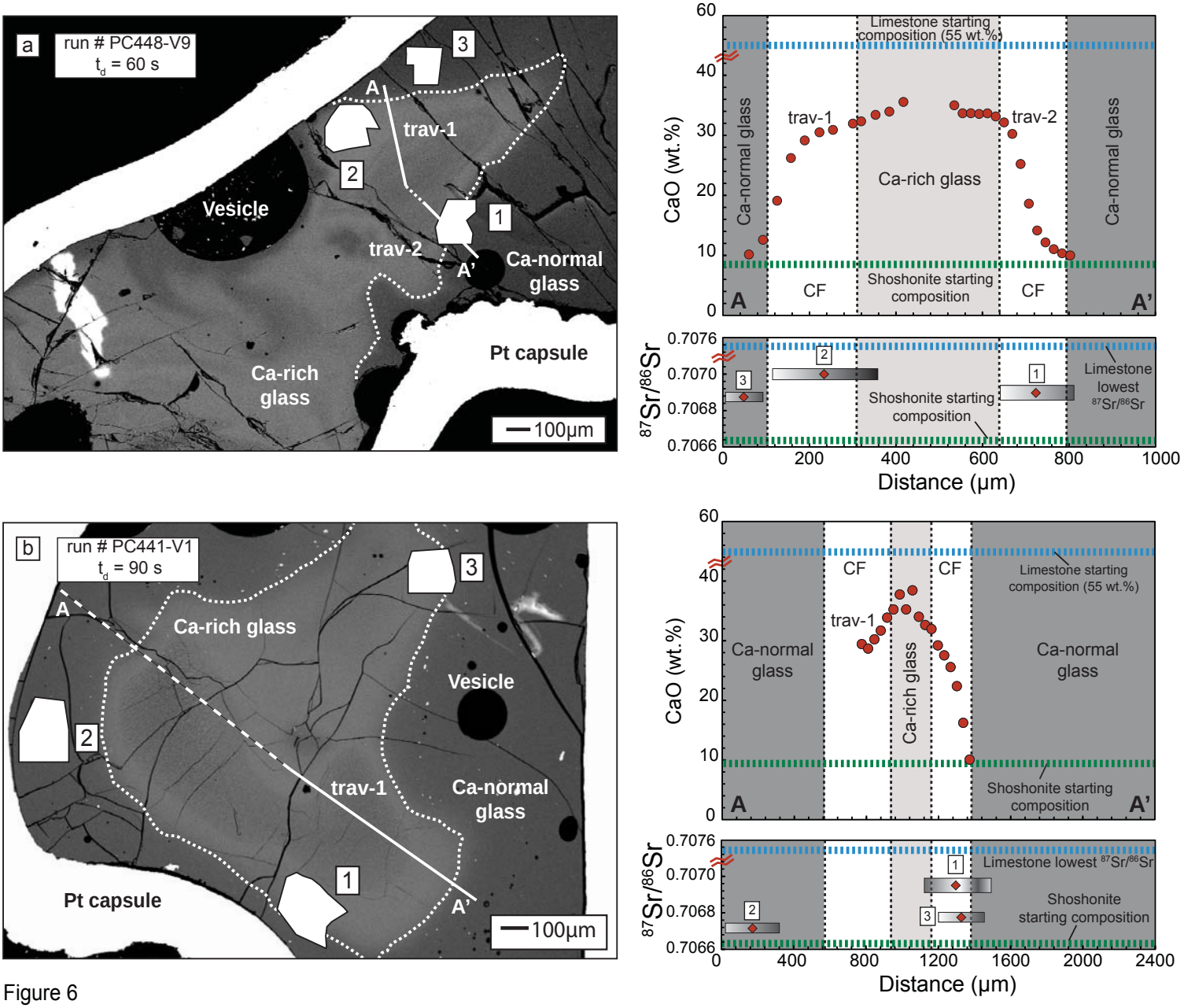
a
run # PC448-V9
t_d = 60 s
A
A'
trav-1
trav-2
Vesicle
Ca-rich glass
Ca-normal glass
Pt capsule
100µm
b
run # PC441-V1
t_d = 90 s
Limestone starting composition (55 wt.%)
Shoshonite starting composition
Limestone lowest $^{87}Sr/^{86}Sr$
CaO (wt.%)
$^{87}Sr/^{86}Sr$
Distance (µm)
CF

Figure 6

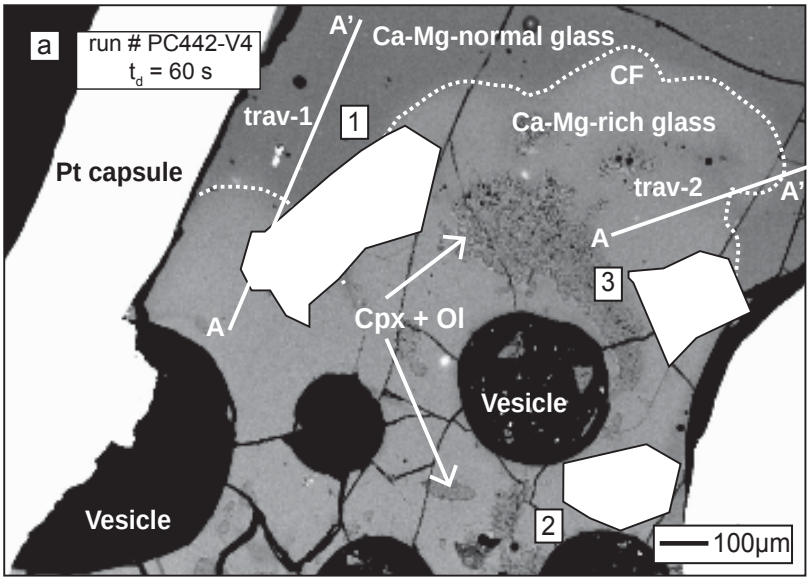
a
run # PC442-V4
t_d = 60 s
A'
Ca-Mg-normal glass
CF
trav-1
1
Ca-Mg-rich glass
Pt capsule
trav-2
A'
A
3
A
Cpx + Ol
Vesicle
Vesicle
2
100µm

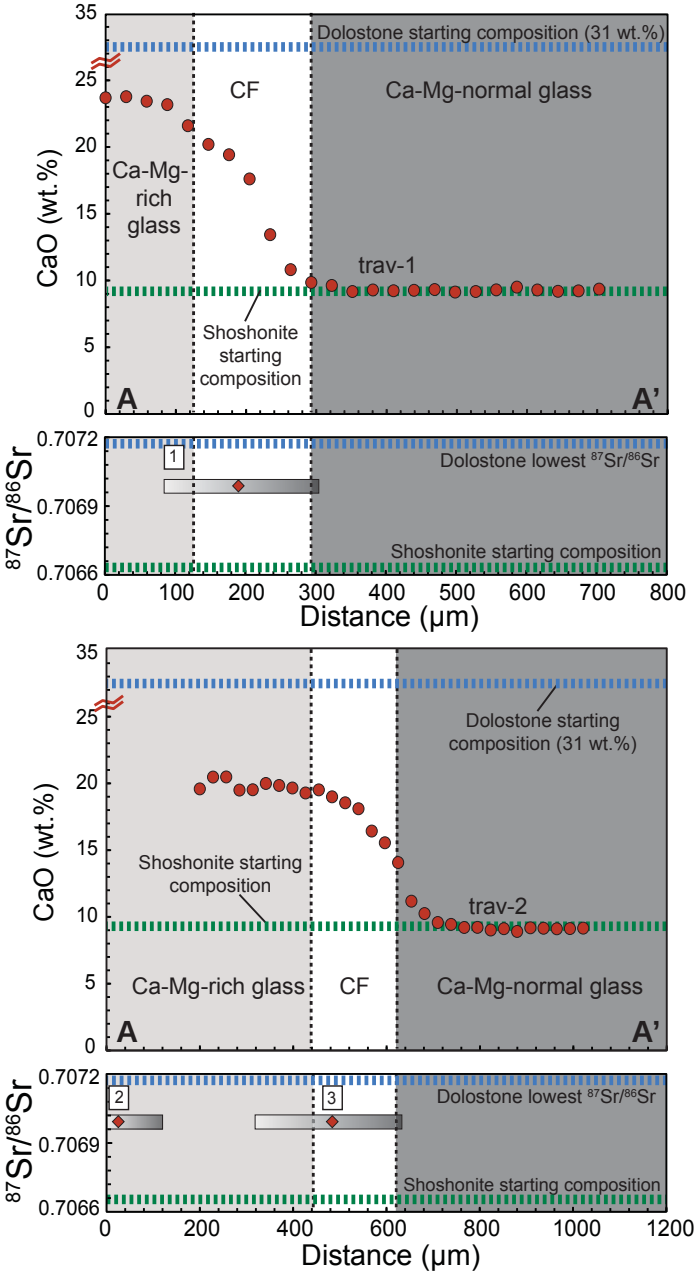
Dolostone starting composition (31 wt.%)
CF
Ca-Mg-normal glass
Ca-Mg-rich glass
trav-1
Shoshonite starting composition
A
A'
CaO (wt.%)
1
Dolostone lowest $^{87}Sr/^{86}Sr$
Shoshonite starting composition
$^{87}Sr/^{86}Sr$
Distance (µm)
Dolostone starting composition (31 wt.%)
Shoshonite starting composition
trav-2
Ca-Mg-rich glass
CF
Ca-Mg-normal glass
2
3
Dolostone lowest $^{87}Sr/^{86}Sr$
Shoshonite starting composition

Figure 7

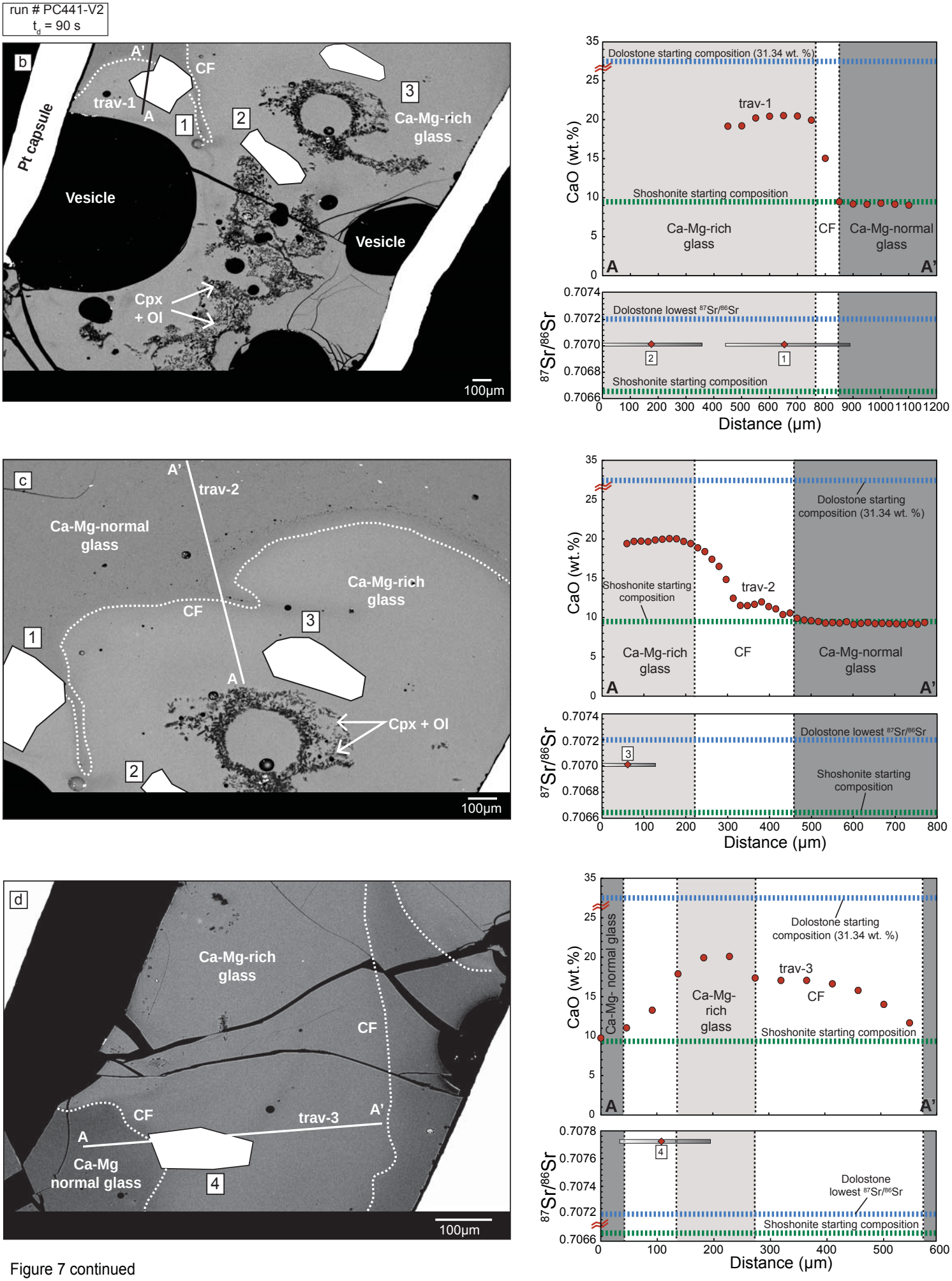

Figure 7 continued

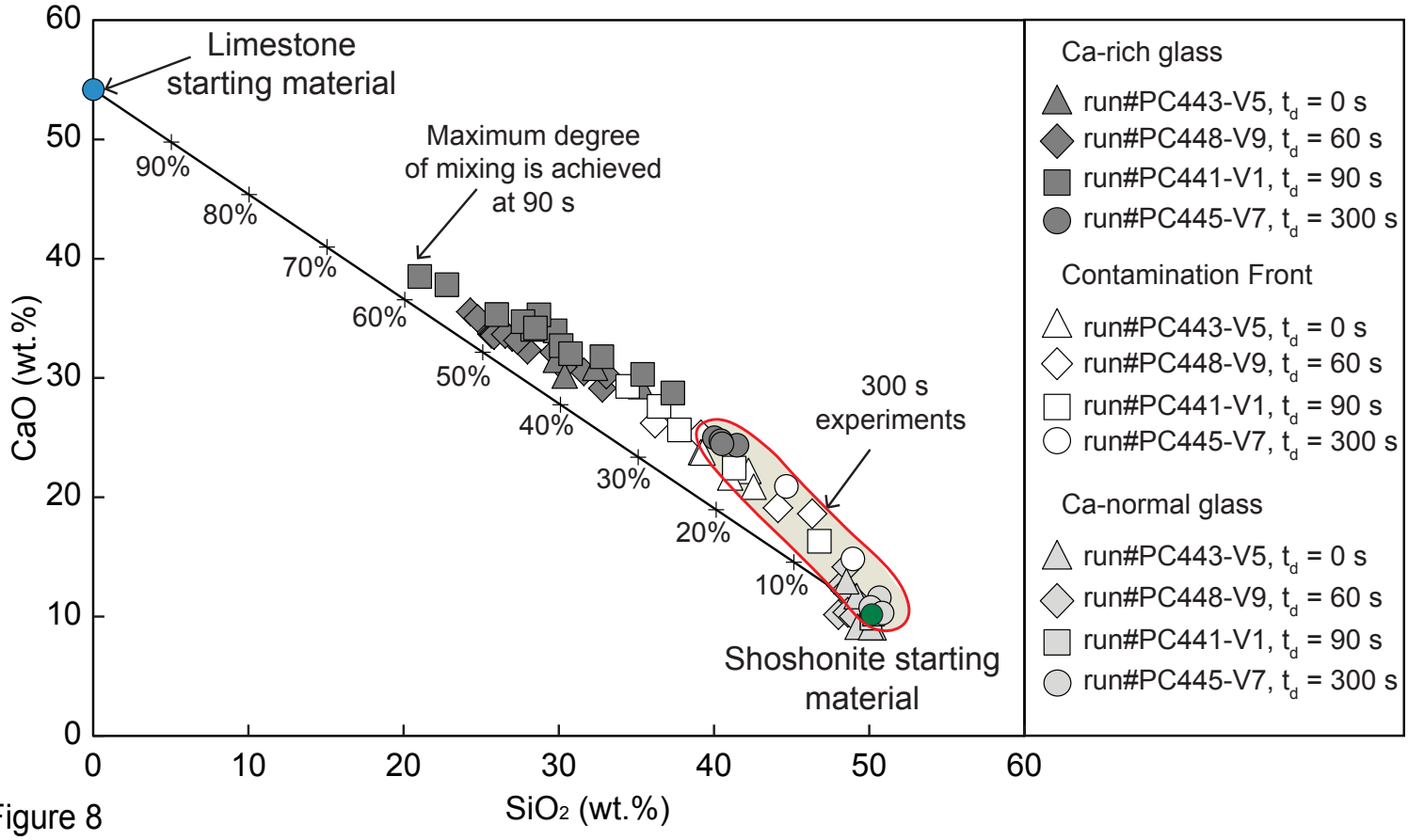
Limestone
starting material
Maximum degree
of mixing is achieved
at 90 s
300 s
experiments
Shoshonite starting
material
90%
80%
70%
60%
50%
40%
30%
20%
10%
CaO (wt.%)
SiO2 (wt.%)
0
10
20
30
40
50
60
Ca-rich glass
run#PC443-V5, td = 0 s
run#PC448-V9, td = 60 s
run#PC441-V1, td = 90 s
run#PC445-V7, td = 300 s
Contamination Front
run#PC443-V5, td = 0 s
run#PC448-V9, td = 60 s
run#PC441-V1, td = 90 s
run#PC445-V7, td = 300 s
Ca-normal glass
run#PC443-V5, td = 0 s
run#PC448-V9, td = 60 s
run#PC441-V1, td = 90 s
run#PC445-V7, td = 300 s

Figure 8

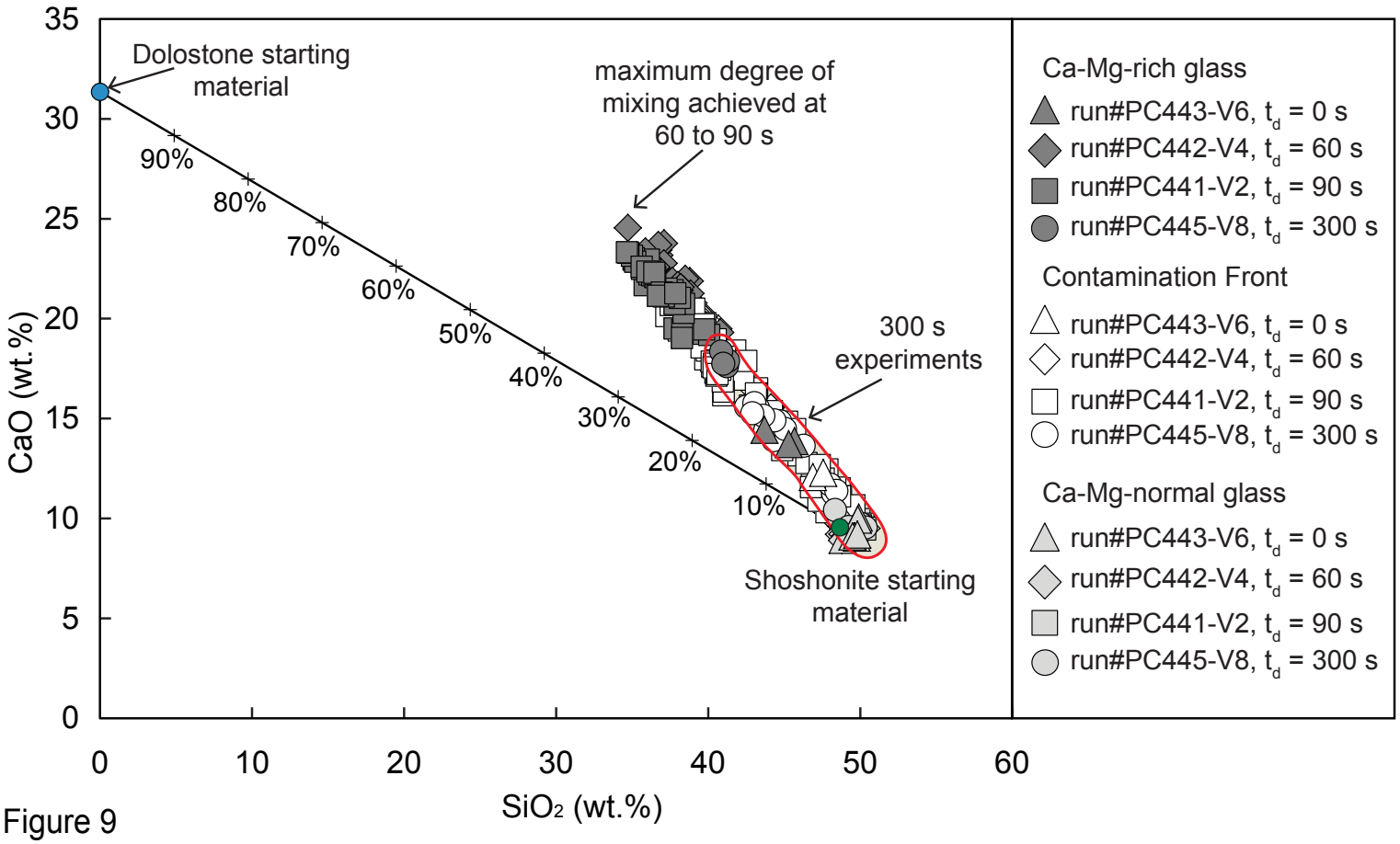
Dolostone starting material
maximum degree of mixing achieved at 60 to 90 s
300 s experiments
Shoshonite starting material
90%
80%
70%
60%
50%
40%
30%
20%
10%
CaO (wt.%)
SiO2 (wt.%)
0
5
10
15
20
25
30
35
0
10
20
30
40
50
60
Ca-Mg-rich glass
run#PC443-V6, td = 0 s
run#PC442-V4, td = 60 s
run#PC441-V2, td = 90 s
run#PC445-V8, td = 300 s
Contamination Front
run#PC443-V6, td = 0 s
run#PC442-V4, td = 60 s
run#PC441-V2, td = 90 s
run#PC445-V8, td = 300 s
Ca-Mg-normal glass
run#PC443-V6, td = 0 s
run#PC442-V4, td = 60 s
run#PC441-V2, td = 90 s
run#PC445-V8, td = 300 s

Figure 9

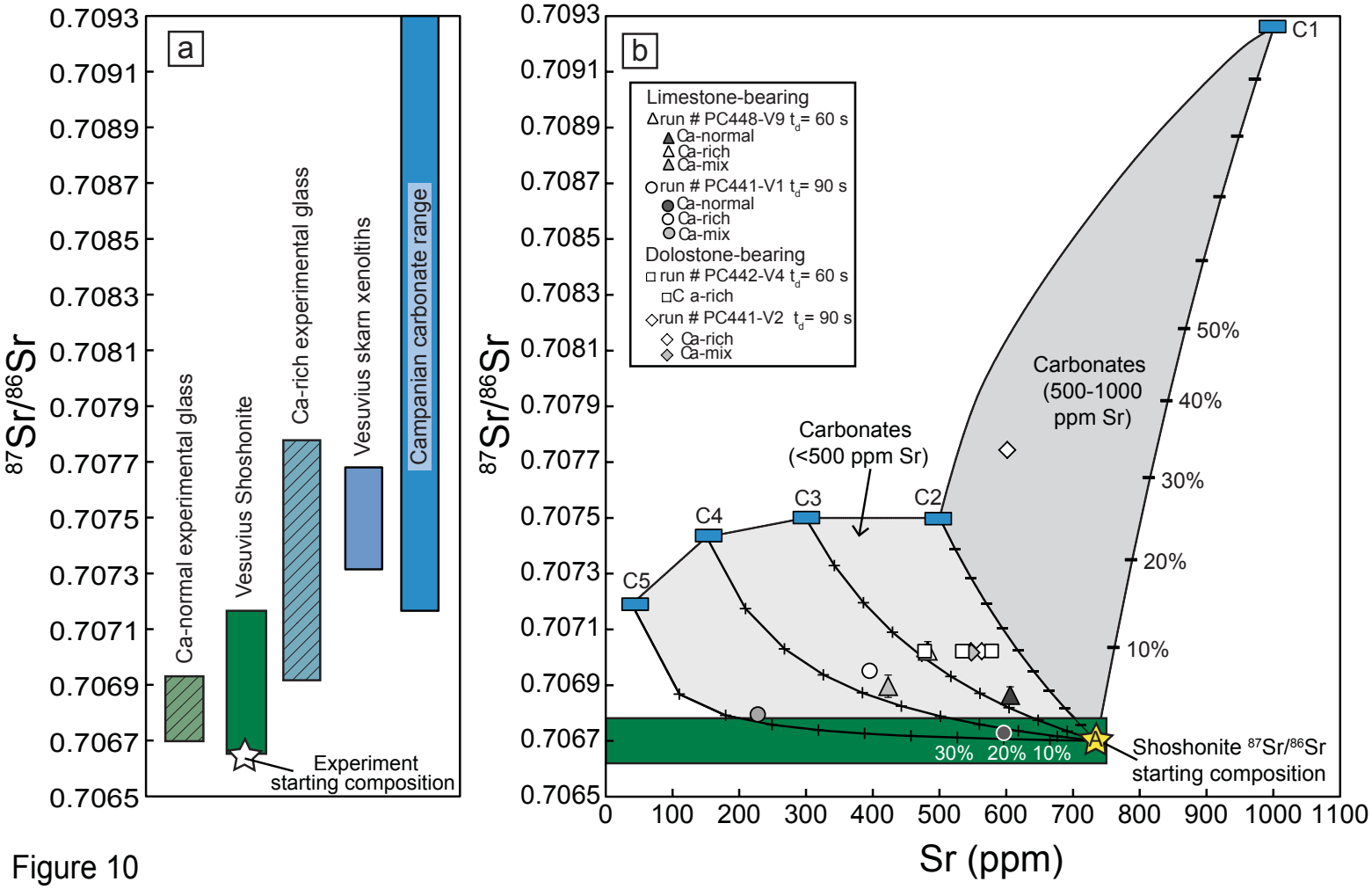
a
b
$^{87}Sr/^{86}Sr$
Ca-normal experimental glass
Vesuvius Shoshonite
Ca-rich experimental glass
Vesuvius skarn xenoliths
Campanian carbonate range
Experiment starting composition
Limestone-bearing
run # PC448-V9 t_d= 60 s
Ca-normal
Ca-rich
Ca-mix
run # PC441-V1 t_d= 90 s
Ca-normal
Ca-rich
Ca-mix
Dolostone-bearing
run # PC442-V4 t_d= 60 s
C a-rich
run # PC441-V2 t_d= 90 s
Ca-rich
Ca-mix
C1
C2
C3
C4
C5
Carbonates (<500 ppm Sr)
Carbonates (500-1000 ppm Sr)
50%
40%
30%
20%
10%
30% 20% 10%
Shoshonite $^{87}Sr/^{86}Sr$ starting composition
Sr (ppm)

Figure 10

Online Resource Table OR1

Electron Microprobe chemical analysis for pyroxene and olivine.
Concentrations are given in mol % as shown in **Fig 3**.

Table 1

Experiment	**PC441-V4 (60 s)**								
	Px 1	**Px 2**	**Px 3**	**Px 4**	**Px 5**	**Px 6**	**Px 7**	**Px 8**	**Px 9**
SiO_2	39.1	39.9	37.3	44.2	44.7	40.2	43.1	44.4	44.8
TiO_2	2.0	2.1	2.1	1.4	1.3	1.3	1.6	1.4	1.3
Al_2O_3	16.4	16.2	17.0	13.1	13.0	17.6	14.2	13.2	12.9
FeO	8.3	7.7	9.8	4.8	4.7	5.0	4.8	4.4	4.5
MnO	0.1	0.0	0.0	0.0	0.1	0.1	0.0	0.1	0.0
MgO	10.7	10.0	10.4	12.7	13.2	14.4	11.8	13.0	13.2
CaO	23.7	25.0	23.0	23.3	23.0	20.7	23.8	23.3	23.3
Na_2O	0.2	0.2	0.2	0.2	0.2	0.1	0.1	0.2	0.1
P_2O_5	0.6	0.7	0.7	0.4	0.3	0.4	0.3	0.4	0.3
Total	101.2	101.8	100.4	100.2	100.4	99.9	99.8	100.3	100.4
Wo	52.60	55.66	50.89	52.19	51.10	46.47	54.19	52.10	51.73
En	33.00	30.97	32.21	39.43	40.74	44.77	37.21	40.31	40.57
Fs	14.41	13.38	16.89	8.38	8.16	8.75	8.60	7.59	7.70

Table 1 *(continued)*

Experiment	**PC441-V4 (60 s)**		**PC441-V2 (90 s)**				**PC445-V8 (300 s)**				
	Ol 1	**Ol 2**	**Ol 3**	**Ol 4**	**Ol 5**	**Ol 6**	**Ol 7**	**Ol 8**	**Ol 9**	**Ol 10**	**Ol 11**
SiO_2	41.0	40.8	40.8	41.7	41.4	41.7	41.1	41.2	41.1	40.2	41.7
TiO_2	0.1	0.2	0.3	0.1	0.2	0.1	0.1	0.1	0.2	0.3	0.1
Al_2O_3	0.8	1.8	0.9	0.6	0.5	0.4	0.7	0.4	0.7	1.1	0.5
FeO	1.7	1.6	1.6	2.6	2.0	2.6	2.2	2.0	1.3	2.5	2.8
MnO	0.1	0.0	0.1	0.1	0.1	0.0	0.1	0.0	0.1	0.0	0.1
MgO	55.2	55.5	55.3	53.9	54.4	55.1	54.7	54.8	54.9	54.3	53.7
CaO	1.8	1.6	1.3	2.1	2.4	1.4	2.0	1.6	1.8	1.9	1.7
Na_2O	0	0	0	0.02	0	0.003	0.012	0	0	0.002	0
P_2O_5	0.07	0.06	0.07	0.02	0.04	0.06	0.05	0	0.02	0.04	0
Total	100.7	101.5	100.3	101.1	101.1	101.4	100.8	100.1	100.2	100.4	100.5
Fo	95.99	96.44	96.70	94.69	94.93	95.72	95.25	96.02	96.35	95.15	94.96
Fa	1.66	1.56	1.57	2.56	1.96	2.53	2.15	1.97	1.28	2.46	2.78

Abbreviations: Px: pyroxene; Ol: O livine; Wo: Wollastonite; En: Enstatite; Fs: Ferrosilite; Fo: Forsterite; Fa: Fayalite

Online Resource Table OR2

Trace element concentrations of drilled micro-samples of experimental glass.

Table 2

	PC448-V9 (60 s)			PC441-V1 (90 s)			PC442-V4 (60 s)			PC441-V2 (90 s)			
Experiment location	**L-V9.1**	**L-V9.3**	**L-V9.2**	**L-V1.1**	**L-V1.2**	**L-V1.3**	**D-V4.1**	**D-V4.2**	**D-V4.3**	**D-V2.1**	**D-V2.2**	**D-V2.3**	**D-V2.4**
Ti^{49}	0.5	0.8	0.6	0.6	0.8	0.3	0.7	0.8	0.9	0.8	0.8	0.9	1.1
Rb^{85}	73.8	122.3	102.7	41.8	155.6	64.2	178.2	170.8	217.7	139.4	121.6	122.5	114.0
Sr^{88}	423.0	605.9	482.3	395.6	596.3	227.7	477.7	534.1	578.1	547.2	563.3	547.8	601.6
Y^{89}	11.4	18.2	19.4	3.2	19.9	7.4	17.4	18.6	23.0	15.6	17.6	19.6	22.1
Zr^{90}	78.0	131.9	101.8	73.4	136.4	51.2	116.6	131.2	143.6	132.3	134.3	133.0	120.3
Nb^{93}	4.7	17.1	11.7	5.4	12.0	6.2	14.2	15.8	12.8	14.3	4.8	7.2	9.7
Ba^{137}	560.2	952.9	712.7	459.5	1107.0	388.9	872.9	899.8	1049.5	932.9	956.3	939.0	941.4
La^{139}	13.6	22.5	41.9	3.6	23.5	8.9	20.7	24.6	35.5	20.4	22.5	27.2	36.1
Ce^{140}	28.6	46.3	43.6	7.5	49.2	18.0	42.9	50.2	58.8	45.8	48.7	49.9	66.3
Pr^{141}	3.8	6.4	10.3	1.0	6.6	2.5	5.9	6.8	9.4	5.8	6.2	7.2	9.7
Nd^{143}	15.7	25.7	40.5	4.2	27.8	10.4	24.2	27.3	36.6	24.0	25.3	29.3	38.6
Sm^{147}	3.4	5.5	6.7	1.0	5.9	2.1	4.9	5.6	7.5	4.9	5.2	6.1	7.3
Sm^{149}	3.6	5.5	7.3	0.9	5.7	2.3	4.9	5.8	7.4	5.0	5.4	6.0	7.7
Eu^{151}	1.0	1.6	1.8	0.3	1.6	0.6	1.5	1.6	1.9	1.4	1.5	1.6	2.1
Gd^{157}	3.4	5.7	7.1	0.9	5.8	2.2	5.0	5.7	6.7	4.7	5.3	5.7	7.2
Dy^{161}	2.2	3.3	3.4	0.6	3.8	1.4	3.3	3.4	4.2	2.9	3.3	3.6	4.1
Er^{166}	1.0	1.6	1.6	0.3	1.6	0.6	1.4	1.6	2.0	1.3	1.5	1.7	1.9
Yb^{172}	0.9	1.5	1.4	0.2	1.5	0.5	1.4	1.4	1.6	1.2	1.4	1.5	1.7

Table 2 *(continued)*

	PC448-V9 (60 s)			PC441-V1 (90 s)			PC442-V4 (60 s)			PC441-V2 (90 s)			
Experiment, location	**L-V9.1**	**L-V9.3**	**L-V9.2**	**L-V1.1**	**L-V1.2**	**L-V1.3**	**D-V4.1**	**D-V4.2**	**D-V4.3**	**D-V2.1**	**D-V2.2**	**D-V2.3**	**D-V2.4**
Lu^{175}	0.10	0.16	0.16	0.03	0.18	0.06	0.14	0.15	0.19	0.13	0.15	0.17	0.19
Pb^{208}	38.98	24.75	18.67	13.48	23.96	7.88	36.85	21.5	38.11	18.71	20.2	20.1	20.46
Th^{232}	4.81	7.69	12.84	1.30	8.13	3.11	7.30	8.08	10.65	6.33	7.22	8.83	10.20
U^{238}	2.41	3.22	2.61	2.53	3.07	1.23	2.71	3.13	3.21	2.94	3.30	3.04	2.68
Tb^{159}	0.01	0.02	0.02	0.00	0.02	0.01	0.02	0.02	0.02	0.01	0.02	0.02	0.02

Concentrations are given in ppm. Location numbers refer to sampled areas in the experiments, as shown in **Fig.5**.

Online Resource 3

Figure OR1. Mixing trends between starting materials in run durations of: 0 s (**a**), 60 s (**b**), 90 s (**c**) and 300 s (**d**) for limestone-bearing experiments. For t_d = 0 and 60 s, the system has locally assimilated up to 40% and 50% carbonate-derived CaO respectively. For t_d = 90 s the system reached its maximum of mixing, being able to assimilate ~ 60% of carbonate-derived CaO. For t_d = 300s, the system has almost homogenised giving an intermediate mixing ratio overall.

Figure OR2. Mixing trends between starting materials in runs at: 0 s (**a**), 60 s (**b**), 90 s (**c**) and 300 s (**d**) for dolostone-bearing experiments. For t_d = 0 s, around 10 - 15% of carbonate-derived CaO has been assimilated. For t_d = and 60 and 90 s, the system reached its maximum degree of mixing of ~ 25-40% of carbonate-derived CaO. For t_d = 300 s, ~ 25% of the carbonate-derived CaO is assimilated in total due to an almost homogenous melt.

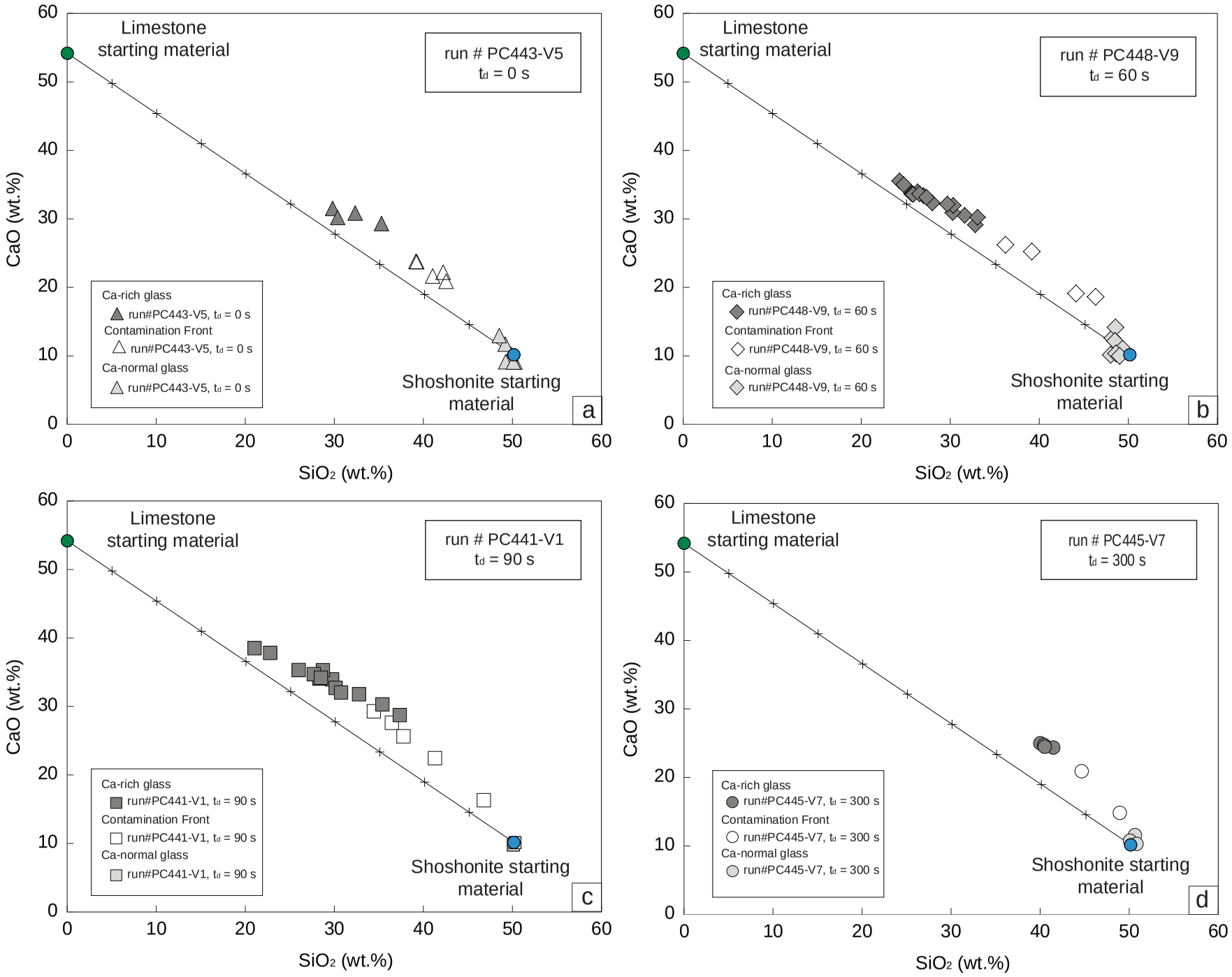

Jolis et al., Online Resource 3 Figure OR1

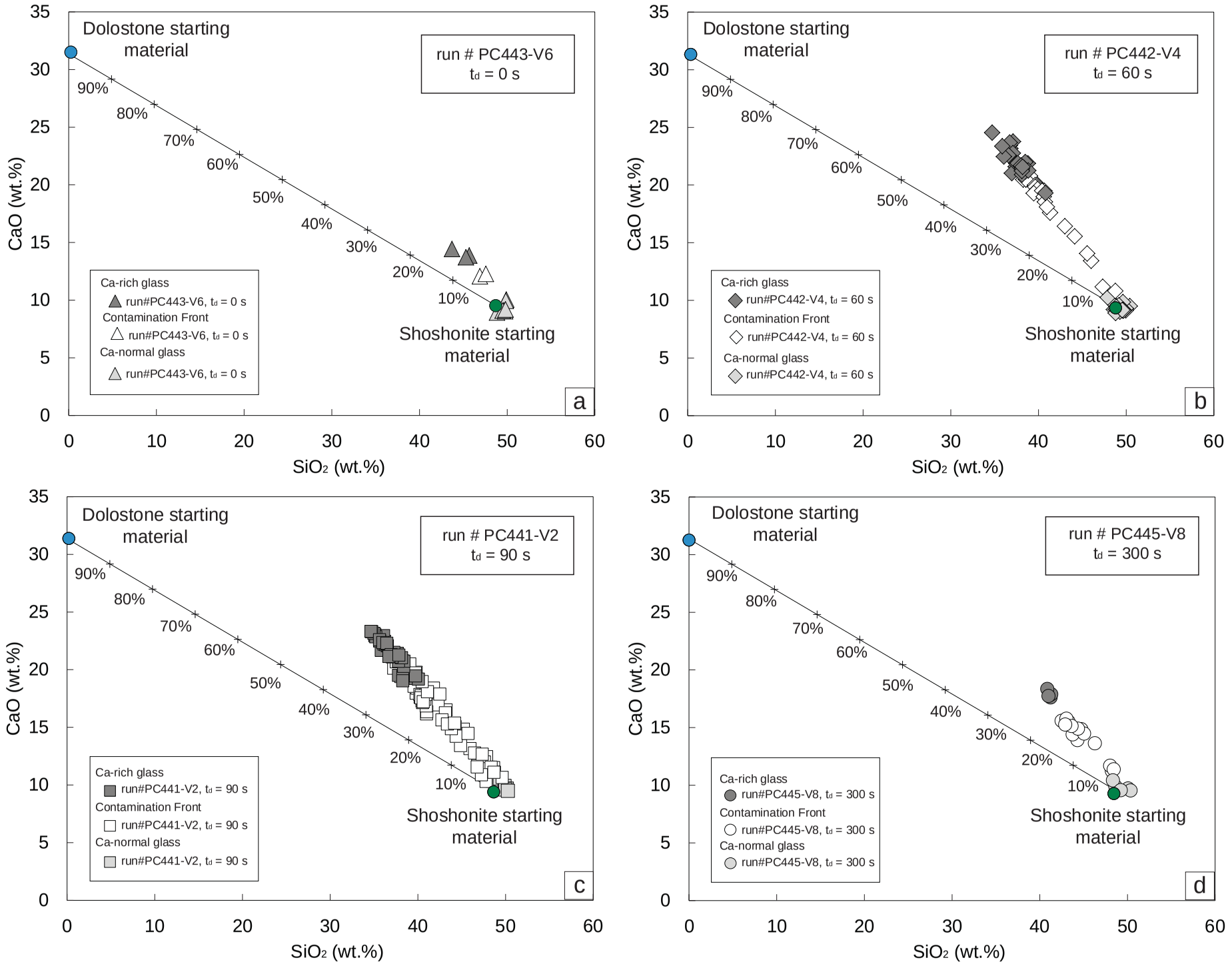

Jolis et al., Online Resource 3 Figure OR2

Online Resource 4

Apparent diffusion coefficients (D) were calculated from the compositional profiles through the limestone-bearing experiments by applying the expression

$$D = x^2/t$$

where D is the apparent diffusion coefficient in m^2/s, x is the location of a specific element along the traverse in meters and t is the experimental time in seconds. This allows us to evaluate the effectiveness of diffusion of an element over a distance across the contamination front and estimate the efficiency of diffusion relative to other processes. The results of these calculations are summarised in **Table OR1**.

Table OR1: *Measured diffusion coefficients*

Limestones							
run#	**T (°C)**	**time (s)**	**Traverses**	**D (m^2/s)**			
				SiO_2	**Al_2O_3**	**MgO**	**CaO**
PC442-V3	1200	60	1	$8.6 \cdot 10^{-7}$	$4.0 \cdot 10^{-10}$	$1.1 \cdot 10^{-8}$	$7.5 \cdot 10^{-9}$
PC448-V9	1200	60	1	$2.0 \cdot 10^{-11}$	$2.0 \cdot 10^{-11}$	$1.8 \cdot 10^{-10}$	$6.3 \cdot 10^{-6}$
			2	$3.9 \cdot 10^{-9}$	$3.9 \cdot 10^{-9}$	$3.9 \cdot 10^{-9}$	$2.0 \cdot 10^{-11}$
PC441-V1	1200	90	1	$2.5 \cdot 10^{-9}$	$1.9 \cdot 10^{-9}$	$2.5 \cdot 10^{-9}$	$4.5 \cdot 10^{-10}$
PC432-V7	1200	300	1	$8.5 \cdot 10^{-10}$	$8.5 \cdot 10^{-10}$	$8.5 \cdot 10^{-10}$	$3.4 \cdot 10^{-11}$